Taylor & Francis
Taylor & Francis Group

International Journal of Hyperthermia

ISSN: (Print) (Online) Journal homepage: https://www.tandfonline.com/loi/ihyt20

In vivo magnetic nanoparticle hyperthermia: a review on preclinical studies, low-field nano-heaters, noninvasive thermometry and computer simulations for treatment planning

Harley F. Rodrigues, Gustavo Capistrano & Andris F. Bakuzis

To cite this article: Harley F. Rodrigues, Gustavo Capistrano & Andris F. Bakuzis (2020) *In vivo* magnetic nanoparticle hyperthermia: a review on preclinical studies, low-field nano-heaters, noninvasive thermometry and computer simulations for treatment planning, International Journal of Hyperthermia, 37:3, 76-99, DOI: 10.1080/02656736.2020.1800831

To link to this article: https://doi.org/10.1080/02656736.2020.1800831

Published online: 10 Jan 2021.

INTERNATIONAL JOURNAL OF HYPERTHERMIA
2020, VOL. 37, NO. 3, 76–99
https://doi.org/10.1080/02656736.2020.1800831

Taylor & Francis
Taylor & Francis Group

In vivo magnetic nanoparticle hyperthermia: a review on preclinical studies, low-field nano-heaters, noninvasive thermometry and computer simulations for treatment planning

Harley F. Rodrigues[a,b], Gustavo Capistrano[a,c] and Andris F. Bakuzis[a]

[a]Instituto de Física, Universidade Federal de Goiás, Goiânia, Brasil; [b]Curso de Licenciatura em Física, Instituto Federal de Goiás, Goiânia, Brasil; [c]Campus Fronteira Oeste, Instituto Federal de Mato Grosso, Pontes e Lacerda, Brasil

ABSTRACT

Magnetic nanoparticle hyperthermia (MNH) is a promising nanotechnology-based cancer thermal therapy that has been approved for clinical use, together with radiation therapy, for treating brain tumors. Almost ten years after approval, few new clinical applications had appeared, perhaps because it cannot benefit from the gold standard noninvasive MRI thermometry technique, since static magnetic fields inhibit heat generation. This might limit its clinical use, in particular as a single therapeutic modality. In this article, we review the *in vivo* MNH preclinical studies, discussing results of the last two decades with emphasis on safety as a clinical criteria, the need for low-field nano-heaters and noninvasive thermal dosimetry, and the state of the art of computational modeling for treatment planning using MNH. Limitations to more effective clinical use are discussed, together with suggestions for future directions, such as the development of ultrasound-based, computed tomography-based or magnetic nanoparticle-based thermometry to achieve greater impact on clinical translation of MNH.

ARTICLE HISTORY
Received 15 April 2020
Revised 4 July 2020
Accepted 17 July 2020

KEYWORDS
Thermal nanomedicine; bioheat equation; cancer; thermal dose; computational modeling; multicore nanoparticles

Introduction

Thermal medicine is an area of research that investigates the benefits of heat delivery for the treatment of diseases. Distinct heat generation technologies are used for this purpose, as for instance radio frequency ablation (RFA), microwave ablation (MWA), high intensity focused ultrasound (HIFU), photothermal therapy (PTT), magnetic nanoparticle hyperthermia (MNH), among others [1]. PTT and MNH has also been allied with nanostructures, where gold and/or iron oxide nanoparticles play a role [2–4]. With PTT, heat generation occurs as a result of the interaction of non-ionizing electromagnetic radiation with the nanostructure, while in MNH the alternating magnetic field (AMF) interacts with the nanoparticle's magnetic moment.

More specifically, one can show, using Maxwell's equations, the first law of thermodynamics, and Poynting's theorem, that for electromagnetic-based heat generators the heat loss ($\dot{Q}$) per cycle is governed by the following equation [5]:

$$\oint \delta\dot{Q} = \int_V \left(\oint \vec{E} \cdot \vec{J} dt - \oint \vec{P} \cdot d\vec{E} - \mu_0 \oint \vec{M} \cdot d\vec{H} \right) dV' \qquad (1)$$

where $\vec{E}$, $\vec{J}$, $\vec{P}$, μ_0, $\vec{M}$ and $\vec{H}$ represent respectively, the electric field, free density current, electric polarization, vacuum magnetic permeability, magnetization and magnetic field. The first term is the free-current loss (also known as eddy current loss), while the second is the dielectric loss, and the third is the magnetic hysteresis loss.

The effect from PTT is due to the second term, where the electric field of the nonionizing radiation can induce electric polarization or interact with a permanent polarization, which depends on the type of nanomaterial utilized. On the other hand, MNH is related to the third term. At low-field amplitudes, where the linear response theory applies, both contributions scale with the square of the field amplitude (electric or magnetic), the frequency and the imaginary susceptibility (electric or magnetic). This is interesting, because it clearly indicates that only if there is an out-of-phase term will heat be generated due to hysteresis (electric or magnetic). This means that $\vec{P}$ and $\vec{M}$ should be out-of-phase with the excitation fields, $\vec{E}$ and $\vec{H}$, in order to generate heat. In addition, the kind of polarization, induced or permanent, will indicate the imaginary susceptibility expression. For example, induced polarizations might be modeled using the Lorentz model (driven harmonic oscillator model), while permanent dipoles might use Debye's model [6]. Obviously, for high field amplitudes, linear response theory (LRT) does not apply anymore, but still the hysteresis argument prevails [7,8].

We also emphasize that the terms 'high' and 'low' field amplitude are strongly related to the anisotropy field (H_k) and the frequency of the external applied AMF in MNH. Some authors claim that deviations from LRT occur for $H > H_k$, while others argue that it becomes clear at $H > 0.2H_k$

CONTACT Andris F. Bakuzis bakuzis@ufg.br Instituto de Física, Universidade Federal de Goiás, Goiânia, Goiás, Brasil

[8,9]. On the other hand, most of *in vivo* MNH studies are performed (see Table 2) at 100 kHz–500 kHz. In this frequency range, the free current loss, that scale with the square of both field amplitude and frequency, needs to be taken into account, since it can be responsible for the nonspecific heat of the patient's body-part exposed to the AMF. This imposes a safety criteria for clinical applications [24–26] and will be properly discussed later in the text. For instance, at 300 kHz one can understand low-field AMF amplitude when $H \leq 16\,\mathrm{kA}.m^{-1}$ (rms values), considering the less strict Dutz-Hergt criteria [25].

Thermal therapies which promote localized heat delivery to target tissues have shown very important applications on oncology, and derive mostly from studies related to synergetic effects with chemo and radiotherapy in the hyperthermia range (40–46 °C) [27]. The biological benefits include the increase in blood flow and vessel permeability during heating (which enhances the oxygenation in the heterogenous tumor microenvironment, thus improving the efficacy of radiotherapy (RT)), accompanied also by an increase in the fluidity and permeability of membranes (which enables the delivery of a higher amount of chemotherapeutic drugs to the cancer cells). Furthermore, heat also affect the DNA-repair mechanism that can induce apoptosis and, even more importantly, might have a great impact in the activation of the immune system [28]. Indeed, the heat-induced immunological response mechanism is still under debate, but it is clear now that both hyperthermia and ablation ($>$ 48 °C) can induce and even improve cancer immunotherapy [29]. Both thermal nanomedicine therapies, PTT and MNH have shown evidence of immune response, in some cases due to the induction of immune cell death [4,13,30]. Nevertheless, the success for such biomedical applications depends strongly on adequately monitoring heat delivery inside the region of interest (ROI), e.g., the tumor and surrounding healthy tissues.

With PTT, more specifically that using gold nanostructures, the magnetic resonance imaging (MRI) thermometry has been successfully applied [31]. Unfortunately, with MNH that uses magnetic iron oxide-based nanoparticles (MIONP), one cannot take advantage of the gold-standard thermometry technique, since the high *DC* field is not compatible with the mechanism of heat generation by hysteresis loss [2,32]. This is still an important challenge to be overcome and might be responsible for the limited clinical applications of MNH. Over the last 10 years, MNH has been approved only to treat brain tumors, when applied together with radiation therapy. There is, as far as we know, no stand-alone MNH therapy application in the clinic, although clinical studies are underway (in 2018 MagForce was approved to start a prostate cancer clinical study using MNH in USA) [33].

The focus of this review is MNH, in particular, we are interested in evaluating the challenges of treatment planning and the monitoring of magnetic nanoparticle ablation applications. In this context, we start by reviewing *in vivo* MNH preclinical studies from the last two decades, with an emphasis on the clinical safety criteria for the application of AMF in humans in order to avoid non-desirable thermal tissue injuries. In this review, we focus on results that use heat alone for the treatment of solid tumors; the combined therapies (radio, chemo, etc) although important, are beyond the scope of this article, but relevant publications on this issue can be found in the literature [23,34–40]. Our study indicates that most of the published results are outside the acceptable clinical range, indicating the necessity for low-field magnetic nano-heaters. Therefore, we include a section reviewing some of the most promising material-based approaches to achieve this goal, where multicore nanostructures, for example nanoflowers, seems to play a role. However, we will show that there is still a lack of *in vivo* studies with such particles. Moreover, in our modest opinion, these material-like strategies alone are not enough to achieve more applications in the clinic, so a section discussing the importance of developing noninvasive thermal dosimetry is introduced. The concepts in this section are very common to thermal medicine scientists, but usually are not adequately considered by colleagues in the materials-like science community. So, one of the purposes of this article is to close the gap existing between such important communities. Anyway, the concepts are crucial for determining the intratumoral thermal dose. With that in mind, we then evaluate several computational modeling articles from the literature about *in vivo* MNH. From this analysis, we identify several limitations on most of the simulations that are due to non-realistic assumptions. This leads us to a discussion about the importance of improving the numerical simulations for *in vivo* MNH treatment planning. Finally, after discussing several limitations of MNH, we point to some future directions that we believe could help to achieve the goal of more effective clinical applications of MNH. These are expected to include not only MNH's great potential as a single platform for tumor ablation, and not necessarily needing to be combined with another standard therapy, but also the three-dimensional localized heat-triggered release of therapeutic agents for enhanced heat-induced immunological responses.

The challenge of real-time and precise determination of intratumoral heating during *in vivo* MNH

MRI thermometry and limitations for MNH

In the clinic, the most important technique for noninvasive temperature monitoring is magnetic resonance imaging (MRI), where the proton resonance frequency (PRF) mapping method is usually preferred [41,42]. This technique has been used in PTT preclinical studies [31] and might be useful in the clinic to monitor prostate cancer ablation, or in other cancers [3]. However, improvements on MRI temperature monitoring might still be necessary since tissue overheating, due to inaccurate magnetic resonance thermometry, has been recently mentioned by the U.S. Food and Drug Administration (FDA) in PTT applications [3]. Independent of that, MRI thermometry for example when used together with HIFU, make this approach the gold standard for thermometry.

On the other hand, MIONPs are excellent MRI contrast agents and they have been extensively investigated with several FDA-approved formulations for improving the diagnosis of a wide range of diseases [43–45], with great emphasis on cancer [46] and cardiovascular illnesses [47], by the more precise detection of primary and metastatic prostate [48] and brain tumors, as well as identifying inflammation, and ischemia [49]. It is natural to expect that MNH will also benefit from MRI thermometry.

Unfortunately, MRI at least with present technology, cannot be used in combination with MNH, because the static magnetic field inhibits the rotation of the magnetic moment of the nanoparticles, and therefore does not promote heat generation [2,32]. Furthermore, the presence of MIONP in biological tissues modifies the magnetic field properties in its vicinity, leading to a dipolar coupling between the magnetic moments of water protons and the magnetic moments of MIONPs, driving a faster dephasing of the water proton spin ensemble, resulting in a lower transversal relaxation time T_2 signal intensity (inversely proportional to the amount of MIONP present) [44]. Since physiological and pathological changes in the tissue environment, due to temperature and viscosity, can also affect MRI T_2-mapping, it is clear that distinguishing the contribution of only the temperature is a very difficult task by this technique, for MIONP concentrations above $1\,mg_{(Fe)}.g^{-1}{}_{(tissue)}$ [50,51].

Moreover, concerning the current clinical applications of MNH, intratumoral injections of MIONP usually use highly concentrated samples (50–100 $mg_{(Fe)}.g^{-1}$ of tumor) [52,53], probably to compensate their low Specific Loss Power (SLP) capacity under a safe and low AMF-amplitude. The presence of MIONP might inhibit the precise delineation of pathological structures, as well as the localization of the nanoparticles within the tumoral mass, due to introduction of image artifacts related to negative contrast, since areas with high concentrations of MIONP appear dark on MRI images [44]. This even compromises the monitoring of the tumor response (growth or recurrence) after the heating therapy due to MNH, since it is only possible to detect tumoral lesions outside the MIONP deposit region [54]. Instead of using MRI, interesting results that determine the localization of MIONP (after intratumoral injection) were obtained using x-ray computed tomography (CT) [55–58], even for the high, greater than $10\,mg_{(Fe)}.g^{-1}{}_{(tissue)}$, concentrations typically applied [51]. Likewise, fluoro-ethyl-tyrosine positron emission tomography/computed tomography (FET-PET/CT) and single-photon emission computed tomography (SPECT) techniques can also be used to monitor tumor evolution in the living organisms after the MNH procedure [54].

At the present moment, real-time temperature monitoring during MNH is obtained using fiber optic thermometers that are invasively inserted inside the tumor [52], but many patients cannot support these probes [59]. Furthermore, this approach reveals only the local temperature and this might not be adequate to judge the success of the heat treatment. In addition, it should be noted that until now MNH therapy is efficiently performed only after the direct intratumoral injection of the nanoparticles, and there are no consistent results reported in the literature using systemic delivery of the nano-heaters to reach target tissues in therapeutic amounts [60]. After intratumoral injection, the nanoparticle distribution depends on several parameters, such as the tumor type (e.g., morphology, vascularization, size, etc.), injection velocity, among others [3,39,57,61]. Several articles in preclinical and clinical studies indicate that the nanoparticles distribute non-uniformly within the tumor [39,52,57,61,62]. Therefore, heat generation is expected to occur heterogeneously within the tumor, which implies that the intratumoral heat dose determination, based on the current clinical approach of using only a few fiber optic thermometers that are invasively inserted inside the patient's tumor [52,53], might not be accurate. Obviously, this approach would limit the clinical use of MNH, since the patient's outcome is strongly dependent on the heat dose delivered [59].

Potential thermometry techniques for in vivo *MNH: limitations and advantages*

So far, clinical studies in MNH have focused mainly on invasively inserting fiber optic thermometers to determine the thermal dose, while in preclinical investigations one can also find surface temperature measurements using infrared thermometry (IRT). Indeed, more recently many preclinical studies have reported the use of infrared thermographic cameras (IR Cam) for monitoring temperature during hyperthermia [45,63–66]. It is a noninvasive imaging technology with promising biomedical applications, which has already been used in the early detection of breast tumors [67–70] and melanoma [71], and thus avoiding unnecessary biopsies. However, this methodology needs to be properly employed or it may result in gross errors in determining the temperature of a region of interest, or even lead to a false positive or a false negative diagnoses, for example, in distinguishing between the heat generated by a precancerous or cancerous lesion and the warming due to the metabolic heat of the healthy tissues around the tumor, or even the difference between heat exchanges due to superficial and deep vascularization [71].

This kind of thermometry, and only in dealing with its noninvasive application, i.e., out of the context of any kind of intraoperative thermal imaging during a surgical procedure [72,73], has the limitation of being employed only for superficial tumors (close to/or at the surface of the skin), as for instance during PTT or MNH of a solid and subcutaneous tumor after having received a direct injection of nanoparticles [23,63–66,74–76]. Moreover, the real intratumoral temperature achieved by the nano-heaters would not be reported but, instead, the surface temperature due to the heat transported from the interior of the tumor to the surface through different tissue layers. Tumors that appear far away from the surface cannot get any benefit from this technology, since heat transport affects the temperature at an organ interface. In spite of these observations, IR technology has the advantage of being noninvasive and is able to monitor the temperature in real-time. However, the challenge is

to correlate the surface temperature measurements with the intratumoral thermal dose due to the hyperthermia/ablation procedure. This limits IR thermometry applications in the clinic, so other accurate thermometry strategies compatible with MNH are necessary.

Indeed, there are other thermometry techniques with MNH under investigation, for example ultrasound thermometry (UST), luminescent nanothermometry (LNT), and magnetic nanothermometry (MNT). Although none of these has achieved clinic use so far, some of them have potential. For example, phantom studies using ultrasound thermal strain imaging (USTSI) during MNH was recently reported [77], but this method might show limitations due to body movements [78]. On the other hand, exploring ultrasound shear wave imaging might be an interesting approach to couple with MNH, since tissue elastic properties are temperature dependent and do not show the limitations of USTSI [78]. Recently, LNT was used during MNH [79] by developing a multicore nanocarrier with MNPs and lanthanide-based nanoparticles embedded in a PLGA matrix. Although this method can perform real-time temperature measurements, this near-infrared optical approach is limited due to the deficient depth penetration of the light. So, it is unlikely that LNT could achieve more robust clinical applications. On the other hand, MNT might be an interesting approach, since the magnetic field does not have this restriction. MNT aims to determine temperature through the measurement of the magnetic response of the nanoparticles under *AC* field excitation, since magnetization is dependent on the temperature as well as on the magnetic relaxation terms (Brownian and Néel). In this case, Magnetic Particle Imaging (MPI) technology together with MNH shows encouraging results [80]. Here, the most promising approach to temperature monitoring might be the analysis of MPI harmonic signals [81]. Another interesting technology that shows great promise for thermometry clinical applications is the computed tomography based thermometry (CTT) [82,83]. However, as far as we know, this technology has not been used with MNH, so the proof-of-concept has not been established yet. Obviously, all those techniques have advantages and limitations. In Table 1 we summarize some relevant information for several thermometry strategies intended to be used together with MNH.

Now it might be relevant to properly define the concept of thermal dose as a valuable tool for the better understanding of the biological effects of heat on cells/tissues. The subject of *in vivo* precise thermometry will be retuned to in our final considerations.

Thermal dosimetry

The analysis of the results found in the literature (*in vitro* and/or *in vivo*), done in order to assess the effects of heat on healthy or neoplastic cells/tissues, must always take into account the time-temperature exposure profile of the heated tissues.

Regarding the use of thermal therapies as adjuvants for cancer treatment, and independent to the heating regime applied (from mild-hyperthermia to ablation), the introduction of an objective thermal dose concept always aims to establish a direct predictive relationship between a number (dose value) and the correlated results of the biological thermal damage caused by heat (e.g., reversible or irreversible functional damage that implies in partial or complete tumor remission, respectively) [90]. The accuracy of any mathematical approach, adopted to calculate the thermal dose value associated with a given biological response, will always be limited to the precision, in real-time, of the intratumoral temperature mapping (where the ideal situation would be its three-dimensional knowledge) of the heat delivered locally [59].

Mindful of the state of the art, it is very important to say that the development of a mathematical approach for the calculation of the thermal dose, which is universally accepted by the scientific community as having predictive value for obtaining a given clinical response, remains an open problem. Because of its importance, it even was the subject of a special closing session (under the title: 'House believes that measurement of thermal dose is essential for thermal therapy') of the 12th International Congress of Hyperthermic Oncology (held in April 2016, New Orleans, LA) and gathered around this debate the most experienced researchers from the Society for Thermal Medicine (STM), European Society for Hyperthermic Oncology (ESHO) and Asian Society of Hyperthermic Oncology (ASHO) [91].

The conversion of the time-temperature exposure profile of heated tissues into a *cumulative equivalent number of minutes* at a temperature of 43 °C, known in the literature as CEM43 [92–94], is the most widely used (but not the only) thermal dose parameter concept employed to predict, or analyze the effects/damages to cells/tissues upon exposure to higher temperatures [59,90,95–97].

Indeed, this kind of proposition remotes to the classic works of Sapareto et al. (between 1978 and 1984) who, by carrying out cell viability experiments *in vitro*, evaluated the effect of temperature and heating time on the capacity of Chinese hamster ovary neoplastic cells (CHO-10B) to continue to replicate their population by forming new colonies. In their studies, the loss of this clonogenic ability due to thermal exposure was identified as an outcome of cell death [92–94]. The survival curves in this kind of experiment are constructed as the logarithm of the ratio of the surviving cell population $S(T)$ (at a given constant temperature T) over the number of clonogenic cells at the beginning of the heating N_0, depending on the heating time interval, that is, the log $[S(T)/N_0] \times t$. In clonogenic cell survival assays like this, cell survival rates $\left(\frac{dS}{dt}\right)$ typically decrease rapidly in the first few minutes of heating (behavior identified as the 'shoulder region' in this kind of graph), distinguished by an increasingly negative slope of the tangent to the survival curve until these rates reach an approximate constant value, resulting from an induced thermotolerance effect, mainly due to the action of heat shock proteins [95].

In this context, defining the hyperthermia time interval as $\tau = (t - t_0)$, a mathematical expression (Equation (2)) was proposed aiming to adjust, even in a limited way, only the part of the survival curve where its slope become constant

Table 1. Potential thermometry techniques compatible with *in vivo* MNH, limitations and advantages.

Technique	Cost	Clinical equipment	Thermometry property	Limitations	Comments
Magnetic Resonance Imaging - MRI	$$$	Yes	$\Delta T = \frac{\varphi - \varphi_0}{\gamma \delta B_0 TE}$; δ is the PRF change coefficient, *TE* the echo time of the gradient echo pulse sequence, φ_0 is the initial phase of the image at temperature T_0, γ the gyromagnetic ratio of hydrogen, B_0 the DC magnetic field of MRI and $\Delta T = T - T_0$ [84].	High DC fields inhibit NP magnetic moment rotation, i.e., inhibit heat generation [2].	Not applicable to MNH, but useful for MNP localization.
Computed Tomography - CT	$$$	Yes	$\Delta T = -\frac{CT(T) - CT(T_0)}{\alpha[1000 + CT(T_0)]}$; where $T(x,y) = 1000\frac{\mu(x,y) - \mu_W}{\mu_W}$; μ_W is the X-ray attenuation coefficient of water, while $\mu(x,y)$ is the average value in the (x,y) voxel, α is the volumetric expansion coefficient, and the *CT* number (also named Hounsfield unit (HU)).	Need to use low dose ionizing radiation for safety concerns [82,83]. Although MNP localization can be determined using this technique, there is still a lack of information about its influence on the temperature dependence variation of CT image.	The method shows great promise for clinical applications if calibration can be performed and CT-based thermometry can be integrated with MNH. As far as we know, so far, there is no study showing the proof-of-concept of CT- MNH.
Ultrasound Thermal Strain Imaging - USTSI	$$	Yes	$\Delta T = \frac{c(T_0)}{2}\left(\frac{1}{\alpha_T - \frac{1}{c(T_0)}\frac{\partial c(T)}{\partial T}}\right)\frac{\partial(\Delta t)}{\partial z}$; α_T is the thermal expansion coefficient, c the sound velocity, Δt the time shifts in ultrasound images due to the temperature change, $\frac{\partial(\Delta t)}{\partial z}$ the thermal strain.	Temperature calibration is strongly influenced by body movement and might show limitations due to image artifacts, animal respiration, etc.	USTSI-based thermometry during MNH was recently demonstrated using phantoms containing MNPs [77]. But there is a lack of in vivo USTSI-MNH studies to check its clinical potential.
Ultrasound Shear Wave Imaging - USSWI	$$	Yes	Monitor the non-linear changes in shear elastic properties of soft tissue that are temperature dependent.	The low frequency mechanical stimulation for generating tissue displacements might depend on MNP distribution in the tumor.	Most promising US thermometry method since the shear wave temperature dependence is not strongly influenced by motion [78]. No proof-of-concept integrating USSWI-MNH.
Magnetomotive Ultrasound Imaging – MUSI	$$	No	Can be used to monitor shear wave propagation due to MNP movement after field excitation. Since elastic properties are temperature dependent can be used as USSWI.	Particle aggregate displacement due to magnetic field excitation might not represent all the MNPs that generate heat. It might be applicable to USSWI-MNH but needs to integrate the field excitation for MUSI and the MNH in a duty-like cycle.	Not applicable to MNH in the present form, although coil design might allow RF excitation. Might be useful to MNP localization [85]. If integrated in duty cycle with MNH might be able to perform USSWI thermometry.
Magnetic Particle Imaging - MPI	$$$	No	Combines the MPI point spread function with a theoretical model that calculates the spatial decay in energy dissipation rates under magnetic field gradients using a phenomenological equation for particles relaxing by the Brownian relaxation [86].	MPI signal was shown to be temperature dependent, but SAR determination assumed particle rotation under ac field excitation (100–500 kHz), which might not contribute significantly to intra-tumoral heat generation.	Powerful technique for MNH that uses gradient fields to excite only specific ROIs inside the body. This has important MNH applications since it avoids heating of undesirable tissues, such as liver or spleen. Proof-of-concept has already been demonstrated [80], and is useful for MNP localization.
MPI Nonlinear Harmonic Ratio - MPINHR	$$$	No	The MPI signal is proportional to the time derivative of the magnetization response, $u_{MPI} \propto \frac{dM(t)}{dt}$. Fourier transform of this signal allows the determination of harmonic terms, $M_{n\omega}(n\omega)$. Temperature can in principle be obtained from the ratio of harmonics after calibration.	Theoretical models usually assume that the NP magnetization response follows the Langevin magnetization, but the time dependence of the magnetization might be more complex. Also, the influence of particle-matrix (biological environment) [87] and particle-particle interaction is not yet well understood and might have a strong influence on the harmonic signal.	Most promising technique for magnetic nanoparticle thermometry since *in vitro* studies suggest that the ratio of harmonic signals does not depend on particle concentration or size distribution [81]. Tuning the excitation frequency for MNP thermometry might be necessary, as well as better understanding of collective relaxation to achieve this goal.

(*continued*)

Table 1. Continued.

Technique	Cost	Clinical equipment	Thermometry property	Limitations	Comments
Luminescent Nanothermometry - LNT	$	No	LNT is based on change of spectroscopic properties with temperature, as intensity in single or pair transitions, peak position shift or lifetime.	Limited to few mm in depth due to optical attenuation, even excited at the biological window. MNPs with potential for LNT are more complex since it also needs a near-infrared fluorescent part.	Might not achieve clinic, although can be used for surface tumor applications. But very interesting for preclinical studies with small tumors. Proof-of-concept of MNH-LNT has been demonstrated [79].
Photoacoustic Tomography - PAT	$$$	No	$\Delta T = \beta\frac{\Delta P}{P}$; where β is a tissue dependent constant, $\Delta P = P - P_0$, with P_0 the photoacoustic signal at temperature T_0 [78].	Limited to few cm in depth. Generally, uses high laser pulsed light, so heat-induced effect might be mixed with laser-induced one. PAT might be useful to localize MNPs but could be limited due to low photothermal conversion efficiency (PCE) of this nanomaterial, at low laser power conditions. Increasing PCE of MNPs might be important to achieve this goal.	Might not achieve clinic because is depth-restricted, but has interesting preclinical applications although still expensive [88]. As far as we know, there is no study showing the proof-of-concept of PAT- MNH.
Infrared Thermometry - IRT	$	Yes	IRT is able to extract temperature information from the detection of thermal radiation phenomena in the infrared region.	Limited to surface temperature determination. i.e., surface tumors. Apparent temperature measurement of curved surfaces is directional dependent and influenced by external temperature [76].	If nanoparticle localization is determined using another technique (e.g., CT, MRI, etc) one might be able to integrate the surface temperature measurements with computer simulations to determine intra-tumoral thermal dose [89]. But not applicable to most clinical situations.

and equal to $-1/D_0$, where D_0 is the needed time (in minutes) for the number of viable colonies to decay to $S = N_0 e^{-1} \cong 36.8\%$ of N_0 [92,93].

$$\frac{S}{N_0}|_t = e^{-\left[\frac{t-t_0}{D_0(T)}\right]} \iff ln\left(\frac{S}{N_0}|_\tau\right) = -\frac{\tau}{D_0(T)} \tag{2}$$

During the *in vitro* hyperthermia experiments with CHO cells, a break in the growth trend of the $1/D_0$ coefficient values was observed due to the increase in the heating temperature to a value near 43 °C, indicating a change in the thermotolerance of these cells, that is, at temperatures $<$ 43 °C the mechanisms of cell death behave differently than what occurs at temperatures $\geq$ 43 °C. Based on these experimental observations, the reference temperature of 43 °C was chosen arbitrarily to convert all thermal exposures to 'equivalent minutes' at this temperature. Thus, Sapareto and Dewey proposed a simple formula to integrate this accumulated dose at a given reference temperature, and the calculation of the thermal dose in the form of the CEM43 can be performed using the equations below [94,95]:

$$CEM43 = \sum_{i=1}^{N} \Delta t_i R_{CEM}{}^{(43-T_i)} \tag{3A}$$

Or

$$CEM43 = \int_0^\tau R_{CEM}{}^{(43-T(t))} dt \tag{3B}$$

Note that the thermal exposure profile can be added either in discrete time intervals (Δt_i) (such that T_i is the average temperature during the heating time interval Δt_i) (Equation (3A)), or in a continuous way (Equation (3B)), where $T(t)$ can even be a function numerically calculated for those cases in which the heating process cannot be easily described mathematically (e.g., the three-dimensional and heterogeneous heat deposit within solid tumors during magnetic nanoparticles hyperthermia). The coefficient $R_{CEM} \cong 0{,}5$ (when $T \geq 43$ °C), or R_{CEM} ranging to 0.125–0.25 (when $T < 43$ °C), are temperature-dependent values obtained experimentally *in vitro* for the CHO cell line and show that, for this murine tumor model, the rate of cell death approximately doubles for each increase of 1 °C above the temperature of 43 °C. However, it is important to emphasize that the authors themselves recognized in their work that the time-temperature relationship upon which this equivalent dose calculation is based (Equation (3A) or (3B)) does not predict, nor does it require, that different cell lines (healthy or neoplastic), as well as different tissues, have the same sensitivity to heat, leading to the same breakpoint temperature at 43 °C [94], as was well demonstrated in the work of S. B. Field and C. C. Morris [98].

Nevertheless, for the ablative temperature regime ($\geq$ 48 °C), where the calculation of the CEM43 has had its accuracy questioned [1,59,95,99], another way to determine the thermal dose delivered is to calculate the thermal damage parameter (Ω). Already in 1947, Henriques and Moritz [100] were the pioneers in interpreting the kinetics of irreversible thermal damage (burning of the skin of pigs and humans

caused by hyperthermia) as an irreversible unimolecular reaction. In their experiments (at constant temperature T) the remaining concentration $C(\tau)$ of viable cells (or undamaged tissues) as a function of the thermal exposure time τ was obtained, relative to the initial concentration C_0 of viable cells/tissues, by the solution of the first-order Bernoulli differential equation (Equation (4)) (below in the text) where k is the overall reaction rate [s^{-1}], i.e., the conversion rate of $C(\tau)$ in cells/tissues permanently injured [95,100]. In this context, an amount of viable cells in their native state C are thermally excited until they surmount an energy barrier $E_a \cong \Delta H^*$ (the enthalpy of activation), forming active complexes CC^* (at a rate k_a), that can relax back (reversible thermal damage) to their native state molecules at rate k_b, or can evolve at an overall denaturation rate k_c to irreversible thermal damage states D [95,99].

$$C \underset{k_b}{\overset{k_a}{\rightleftharpoons}} CC^* \overset{k_c}{\rightarrow} D \iff -\frac{dC(\tau)}{dt} = kC(\tau) \iff \frac{C(\tau)}{C_0} = e^{-\int_0^{\tau} kdt} \tag{4}$$

The temperature-dependence of k, according to the Eyring-Polyani equation (used in chemical kinetics theory) to describe changes in the absolute rate of a chemical reaction against temperature, can be calculated as:

$$k(T) \cong Ae^{\left(\frac{-E_a}{RT}\right)} \tag{5}$$

where A [s^{-1}] is the frequency of effective collisions between reacting molecules in the bimolecular reaction model, $R = 8{,}3143$ [J.mol^{-1}.K^{-1}] is the universal constant of ideal gases and T is the temperature at which cells/tissues are kept for the time t [95,99].

Moreover, from Equations (4) and (5) the thermal damage parameter Ω is obtained as:

$$\Omega = ln\left[\frac{C_0}{C(\tau)}\right] = \int_0^{\tau} kdt = \int_0^{\tau} Ae^{\left(\frac{-E_a}{RT(t)}\right)} dt \tag{6}$$

Basically, for discussion of hyperthermia CEM43 is the most used thermal dose parameter, while for ablation the thermal damage parameter Ω is chosen. In a recent review, Gerard C. van Rhoon has discussed the relevance of the calculation of CEM43 as a predictive parameter of biological outcomes for *in vivo* thermal therapies applied to cancer treatments [59], since the thermal dose value obtained *via* Equation (3A) or (3B) has major intrinsic limitations, as follows. First, Arrhenius-type mathematical modeling fails, in many, but not in all cases, by overestimating the rate of cell death in the first minutes of *in vitro* mild hyperthermia (in the range of 43–46 °C) of neoplastic cells, that therefore can lead to overestimating the thermal damage thresholds [59,101]. And, as already mentioned earlier, Equations (3A) or (3B) can adjust only the linear part of the survival curve, ignoring the 'shoulder' of the cell survival curve and not reporting any parameters associated with the transient region related to the process of induced thermotolerance [99,102]. Second, both in the calculation of the CEM43 or of Ω in the Arrhenius model (Equation (6)), the cell death rate accounts only for the loss of clonogenicity as a function of temperature and heating time. However, the process of cell death by hyperthermia is much more complex, intricate and not yet fully elucidated. Involving, in addition to the loss of clonogenic ability, multiple parallel processes of thermal damage already identified in the literature: e.g., cascade of caspases that result in the induction of apoptosis, necrosis, necroptosis, irreversible functional damage to both cell and nuclear membrane, and to the cytoskeleton [59,95].

John A. Pearce has already proposed in the literature more than one multi-parameter adjustment method (with analytical and also numerical solutions) modeling cell survival data due to multiple parallel processes of thermal damage [95,102], in addition to discussing in-depth relevant proposals from other authors, including a model for the calculation of a coefficient quite equivalent to the parameter of thermal damage Ω for the ablative temperature regime $\geq$ 48 °C [1,95,99]. So, we suggest that the readers access the cited publications for more sophisticated discussions regarding thermal dosimetry. Further, although the importance of thermal dose is well established in the clinic, you will notice in the discussions below that most of the MNH reports in the literature, such as from preclinical studies, do not report this adequately.

In vivo MNH: clinical safety criteria and preclinical results prospecting MNH's benefits as a single therapeutic platform

The idea of using the phenomenon of hysteretic dissipation in magnetic materials to generate heat and treat cancer is not new; surgeon Robert Gilchrist et al. (at St. Luke's Hospital, Chicago, IL) published in 1957 the results of a pioneering *ex vivo* study in dogs with spontaneous metastatic colorectal carcinoma. Since the surgical resection of the tumors of these dogs was not able to eliminate the metastases developed in the lymph nodes of the retroperitoneal tissue, the researchers made injections in different regions affected by the tumor in the dogs' bodies (subserosa bowel, subcutaneous and subperitoneal tissues), using a poly-dispersed magnetic fluid containing γ-Fe_2O_3 nanoparticles (ranging from 20−100 nm). The injected area and lymphatic drainage area (with concentration of 5 $mg_{(Fe)}.g^{-1}$ of lymph node) were removed *en bloc* and exposed to a varying AMF in the range of 15.9−19.0 kA.m^{-1}, at a fixed frequency of 1.2 MHz, promoting a temperature rise of 14 °C (in 3 min of application) measured with an alcohol thermometer (too big to be introduced into the tumor with the live animal). In their conclusions they highlighted considerations for future *in vivo* treatments, the need for improved magnetic characteristics and the smaller size of the particles in order to reach a therapeutic heating regimen by better filling of the lymph nodes with the nano-heaters delivered *via* the lymphatic system. In addition they mentioned the need to improve the AMF setup for *in vivo* applications, aiming to raise the temperature of any part of the body for either a few seconds or for prolonged periods, avoiding undesirable thermal injuries due to nonspecific heating by eddy currents [103].

The realization of *in vivo* MNH offers some unique technical challenges and it is very interesting to note how the problems identified by Gilchrist had already ranked some of the main (and still current) difficulties regarding definitive implementation of the MNH procedure as part of the standard of care for cancer treatment [104].

Firstly, the systemic delivery of magnetic nanoparticles has not been successfully achieved. Murine xenografted solid tumors usually grow much faster than most human tumors [105], with intensive angiogenesis, creating a dense and defective vascular architecture (with intercellular fenestrations ranging 100–780 nm). It results in an impaired lymphatic drainage system that is believed to favor structures of about 100–150 nm, allowing them to be entrapped and retained within solid tumors at high concentrations for prolonged periods (more than 100 h) while, due to the high-pressure gradient in the interstitial space, low-molecular-weight substances can return to the circulating bloodstream by diffusion. This dynamic behavior of macromolecules and lipids in solid tumors is called the Enhanced Permeability and Retention (EPR) effect which is believed to favor the passive delivery of nanocarriers to the tumor [106,107]. It was extensively studied during the last three decades, but currently the EPR effect has been subject to intense debate, since this mechanism could not be consistently observed in humans, while it is active in rodents [105].

Likewise, in the last three decades, a great variety of nanocarriers has been developed (in a wide size range, from 1 to 1000 nm) mostly functionalized with biomolecules (e.g., folic acid, antibody fragments, molecular ligands, protein receptors, antineoplastic agents, etc.) in order to increase the uptake of these nanocarriers by the target cells (active vectorization) for labeling, imaging and controlled drug delivery at the cellular level [14,108,109]. However, up to date studies like the one reported by Wilhelm et al. indicate a systemic delivery efficiency with a median of only 0.7%. This relevant review evaluated nanoparticles used in 232 reports published from 2005 to 2015, which dealt with their passive (175 articles) or active (56 articles) vectorization for solid tumors [60]. More recently, it was shown that the inter-endothelial gaps, that were believed to be responsible for nanoparticle delivery through the EPR effect, are not in fact mainly responsible for the delivery of nanoagents [110]. On the contrary, active processes seem to dominate, which suggests that new nanoparticle designs that take into account biological processes are necessary to improve the delivery of therapeutic agents with the help of nanoparticles. Consequently, until now, it has not been possible to perform MNH in a therapeutic manner using systemic delivery of the magnetic nanoparticles, since macroscopic heating is a collective effect and requires a minimum number of heat centers to occur [111,112].

Another important issue for the adequacy of MIONPs aiming the success of *in vivo* MNH concerns about determining the biocompatibility of MIONPs, since it refers to the ability to perform the function for which it was designed, generating a more beneficial cell/tissue response without causing adverse local or systemic health effects on the host organism [113,114]. As the presentation of MIONPs formulations are colloidal suspensions, the nanoparticle's surface covering and passivation in order to avoid aggregation (e.g., with surfactants or long-chain polymers), or even its functionalization for targeting delivery, can also improve their biocompatibility by increasing their resistance to lysosomal acidity [115]. In addition to a great variety and combination of factors related to the MIONP's structural properties, chemical composition, size, solubility, route of administration, dose, biodegradability, pharmacokinetics, and biodistribution play a role [116,117]. For instance, in the case of drug nanocarriers, biocompatibility is directly linked to the response of the immune system after its administration and also to the toxicity of the drug carried and/or of its biodegradation metabolites [116]. For this reason, factors such as magnetic core materials, their biodegradation products and clearance are important from the point of view of the biocompatibility of magnetic nanocarriers [118].

Indeed, another reason for the lack of effective systemic delivery of magnetic nanocarriers to target tissues (where most pre- and clinical studied materials are in the range size ~10–300 nm) is about their accumulation, after being taken up by macrophages in bloodstream circulation, liver, spleen, lymph nodes [119–121]. This off-target load can be far more than the tumor itself, and the body exposure to an AMF could result in collective heating that might inflict damage to these vital organs [122]. It has already been demonstrated in the literature that when the MIONPs underwent the progressive body metabolism resulting in its magnetic core degradation, the iron content released is incorporated into the body's iron store and is progressively found in red blood cells (hemoglobin), and ultimately eliminated very slowly, predominantly *via* the feces, i.e., through hepatic clearance [121]. Indeed, now is well established that particles smaller than around 5 nm are eliminated from the body through renal clearance, while larger ones use the hepatic clearance route [123]. In most applications using MIONPs the particle sizes are larger than 10 nm, but during biodegradation diameter might be reduced and some smaller nanoparticles could be eliminated through renal clearance [124,125]. In the case of applications with distinct ferrites, the ions eliminated from biodegradation might also be an important toxicity parameter that should be controlled by tuning the amount of magnetic material administrated in the body. One can also improve the biocompatibility by surface passivation process, as for example enhancing the nanoparticle surface with iron that can result in a core-shell nanostructure.

Second, there is difficulty in establishing the threshold for safe AMF application. Unlike what is the case in the MRI imaging technique, where there are well-established guidelines provided by the FDA [126], as well as by the International Commission on Non-Ionizing Radiation Protection (ICNIRP), to support its safe use in medical applications [127], there still are no ground rules with clearly defined safety criteria for the use of AMF in the context of *in vivo* MNH. In most of the preclinical and clinical results published, the product (field amplitude $H \times$ frequency f) equal to 4.85×10^8 A.m^{-1}.s^{-1} is the most widely used (but

not the single accepted) threshold for *in vivo* safe applications of *AC* induction fields, above which it is expected to be harmful to the patient's health [109]. This criterion was defined by Atkinson et al. after clinically evaluating reports of subjective feelings of discomfort and pain due to intense heating, in patients whose thorax (radius $\sim$ 15 cm) was surrounded with a single-turn induction coil that underwent an AMF (of varying intensity) with a constant frequency of 13.56 MHz. In their results, they concluded that the product value $Hf = (35.8\,\mathrm{A}.m^{-1})\ (13.56\times10^{6}\,\mathrm{Hz}) \cong 4.85\times10^{8}\ \mathrm{A}.m^{-1}.s^{-1}$ was thermally tolerated by humans for extended periods of time [24]. But, depending on the duration of AMF exposure time, the accompanying temperature rise can provoke serious adverse health effects, as reported by Oleson R.J. that non-localized thermal transfer due to eddy currents can cause blisters to form on the skin when this limit is exceeded [109,128].

It should be noted that the patient's exposure time is a relevant criterion to consider for defining the safe limits of AMF *in vivo* applications, mostly when considering experimental protocols that demand consecutive heating inductions [76]. As the tissue thermal load increases due to AMF prolonged exposure, its effect remains mainly at the dermis level since eddy currents are directly proportional to the cross-section radius of the body-part irradiated [24] and thermoregulatory functions such as vasodilation and sweating play a role to restrict a body core temperature rise, even though the extensive vascular network within the dermis can transport this heat deep within the body [129].

Most of *in vivo* MNH is usually performed in the frequency range 100–500 kHz (see Table 2) with few applications reaching up to a few MHz, i.e., in the low-Radio Frequency (LRF) bandwidth. This confers to MNH the advantage that it might be effective for the treatment of deep tumors (with a depth larger than 4 cm or situated centrally in the body), thus avoiding invasive procedures. With other electromagnetic-based thermal therapies, such as MWA and RFA which operate at higher frequencies (commonly from 400 MHz to $\sim$3 GHz), the penetration depth into tissues is short (up to 3–4 cm) relative to the body-part dimensions. Consequently, the specific absorption rate (SAR) of power by the tissues becomes more superficial (restricted to the near-field zone) relative to its distance from the electromagnetic field (EMF) source (*i.d.* attenuates rapidly away from RF electrodes and optical fibers) [1]. In contrast, for the human torso (modeled as a cylinder of real dielectric material with radii up to 0.15 m), exposure to an external AMF at frequencies up to 13.56 MHz resulted in a field intensity at the axis of the torso model of 92% of the surface value, but for slightly higher frequencies this percentage drops rather rapidly to less than 40% [130].

It is fair to say that the current ICNIRP limits for human exposure to EMF in the wide-radiofrequency range (100 kHz–300GHz) are far more protective against thermal hazards than recommended earlier by Atkinson, since the basic premise now is that body core temperature should not rise by more than 1 °C for extended periods of time ($\geq$30 min). This guideline also states that the whole-body SAR should not exceed 0.4 $\mathrm{W.kg}^{-1}$ (averaged over an entire body mass of 70 kg and a 30-min interval) and, in the case of partial body exposure, the local SAR should not exceed 10 $\mathrm{W.kg}^{-1}$ (for head and torso) and 20 $\mathrm{W.kg}^{-1}$ (for limbs), both quantities averaged over 10 g of tissue, also for a 30-min interval [127]. Very conservative positions were also recommended: 41 °C as a threshold for potentially harmful effects from local heat-induction [127], based on a substantial body of literature [90,96,131] and, in order to avoid discomfort and pain, ICNIRP also suggests reference levels of AMF amplitude (rms value of *H*-field) of up to only 100 $\mathrm{A}.m^{-1}$ (when $f = 100$ kHz) and up to 10 $\mathrm{A}.m^{-1}$ (when $f =$ 1 MHz), resulting in a threshold of $Hf = 10^{7}\ \mathrm{A}.m^{-1}.s^{-1}$ [127], i.e., around 50 times lower than the previous Atkinson criteria.

Maier-Hauff et al., using the first clinical AMF applicator for humans, published results from a Phase I clinical study involving 14 patients (median, 55 years old) with recurrent glioblastoma multiforme (GBM). These patients were submitted to 6 sessions of MNH (60 min each one) with magnetic field strengths up to 13.5 $\mathrm{kA}.m^{-1}$ (at a constant frequency of 100 kHz) that were tolerated well by all of the patients [53]. According to Dutz and Hergt in their review articles [25,26], this clinical result is evidence that the given Atkinson threshold might be 10-fold exceeded for *in vivo* applications of MNH treatment, indeed they suggest a new safe limit of $Hf \leq 5\times10^{9}\ \mathrm{A}.m^{-1}.s^{-1}$ (if the coil applied has a typical diameter around 10 cm).

However, as pointed out by Kozissnik et al., the establishment of a clinical safe limit should not be performed without taking into account the intrinsic dependence of the skin's electrical conductivity (σ) value, which can vary significantly in function of the frequency of the externally applied AMF [109]. For instance, modeling the skin as a real dielectric medium, using the condition in which the Atkinson criterion was determined (with the AMF frequency $f = 13.56$ MHz) the electrical conductivity of the dry human skin corresponds to $\sigma \cong 0.238\ \mathrm{S}.m^{-1}$ (in SI units: one Simiens corresponds to $[\mathrm{S}] = 1\ \mathrm{A}^2.\mathrm{s}^3.\mathrm{kg}^{-1}.m^{-2}$). Comparatively, if we consider the value of 100 kHz used for humans treatments, then this same parameter falls three-orders of magnitude to $\sigma' \cong 4.513\times10^{-4}\ \mathrm{S}.m^{-1}$ [132–135]. In this context, it should be noted that according to Atkinson's own expression for the non-localized heat loss power (P_{eddy} [W]) generated by eddy currents, where $P_{eddy} \propto \sigma$ [24] and, if the Atkinson's experiment were performed at 100 kHz (the same frequency of the AMF applicator for humans), then the new limit that would need to be exceeded in order to produce the same value of P_{eddy}, which can result in pain, or even worse, in irreversible thermal damage of the skin, would be equals to $H'f' = \sqrt{\frac{\sigma}{\sigma'}}\cdot(4.85\times10^{8}\ \mathrm{A}.m^{-1}.s^{-1}) \cong 1.11\times10^{10}\ \mathrm{A}.m^{-1}.s^{-1}$.

Nevertheless, during the clinical use of MNH, there is no report in the literature that such a high value ($Hf \sim 10^{10}$) is well tolerable by patients, although it has already been observed that the safe limit of the AMF amplitude and frequency varies for different regions of the human body. For example, at a fixed frequency of 100 kHz, it was found that for the pelvic region the tolerable limit value is 6 $\mathrm{kA}.m^{-1}$

(resulting in $Hf = 6 \times 10^8$ A.m^{-1}.s^{-1}); for thoracic and neck region up to 7.5 kA.m^{-1} ($Hf = 7.5 \times 10^8$ A.m^{-1}.s^{-1}) and for head/brain up to 13.5 kA.m^{-1} ($Hf = 1.39 \times 10^9$ A.m^{-1}.s^{-1}) [136].

Evidently, the above calculations are only estimates illustrating the fact that, probably, a safety limit for the use of AMF (in the context of MNH) should be established based on clinical results, such as those presented by Atkinson and Maier-Hauff, but not without taking into account the experimental specificities of each assay (e.g., the dimensions of the coil used, intensity and frequency of the applied inductive field, the electrical conductivity of the excited tissues, etc.).

Unfortunately, to date, exclusive heat delivery applications using the MNH technique for cancer treatment in the clinic has not yet been achieved. For instance, it would be desirable to investigate the potential of MNH for the ablation of deep seated tumors (without recourse to invasive procedures), relying only upon the effect of the heat generated by hysteresis. This could be done from the analysis of preclinical investigations in order to build a better theoretical framework and to investigate a number of relevant experimental parameters that would permit optimization of the technique and lead to a future clinical translation.

In this regard, it can be seen in Table 2 (below in the text) that preclinical studies demonstrating the effectiveness of hyperthermia using MIONP started basically in the late 1990s. Jordan et al. published results using magnetite-based nanoparticles, with dimension of (3.1 ± 0.7) nm (and SLP = 160 W.$g^{-1}_{(NP)}$), in an AMF setup of 520 kHz and varying intensity 6–8 kA.m^{-1} (≅ 75.4–100.5 Oe). The *in vivo* model studied was a solid, subcutaneous tumor of C3H (mammary carcinoma) induced in mice ($n = 13$; $V = 120$–400 mm^3), where each treated animal received 4.2 $mg_{(Fe)}$ (averaged over 400 mm^3 of tumoral tissue) injected intratumorally. The animals were treated only by MNH for 30 min and the average intratumoral temperature was (47 ± 1) °C about 25 min during the *in vivo* procedure. The treated animals were monitored for a period of up to 60 days. When compared to the control (untreated animals), the decrease in the tumor growth rate of mice after MNH treatment is clear, with partial tumor remission (PR) in 44% of the mice that underwent thermal therapy. In addition, there appeared to be animals with apparent complete tumor remission (CR), although this biological response is not highlighted in the paper [10].

In 2001, Hilger et al. [11] investigated the possibility of thermal ablation using magnetite nanoparticles (10 nm and 211 W.$g^{-1}_{(NP)}$). The murine tumor model was MX-1 ($n = 10$ mice). Intratumoral temperatures of up to 70 °C were reported from 4 min treatments with an applied AMF intensity equal to 6.5 kA.m^{-1} (≅81.7 Oe) and a frequency of 400 kHz. In this case, 21 mg of magnetic material was injected intratumorally. All the animals were sacrificed after the treatments and the histologic sections of the tumors analyzed revealing irreversible thermal damages due tumoral heating (early stages of coagulation necrosis, with predominant nuclear degenerations).

A few years later (in 2006) Ito et al. [13] investigated the effect of the magnetic hyperthermia using magnetoliposomes, which consist of vesicles (∼ 150 nm) containing nanoparticles of magnetite inside. The group reports studies on several tumor models B16, MM46, Os515, Vx-7 and T-9. In particular, in the last model (glioma), the study consisted of the induction of two tumors (located in diametrically opposite positions in the mouse's abdomen) followed by applying an AMF of 30.6 kA.m^{-1} (≅ 384 Oe) and 118 kHz. Magnetic nanoparticles were injected in only one of the two tumors and, according to the authors, in some cases on the 28th day after the treatment by MNH a complete remission of both tumors of the animals had occurred (see Table 2), i.e., the authors observed an abscopal effect [40,137–140]. Killing tumor cells with heat also induced a strong host immune response. Overexpression of heat shock proteins by neoplastic cells during hyperthermia influenced antitumor immune responses, according to the authors. More recently, some new studies have discussed the heat dose effect, in which a treated tumor acts as a sensitizer to boost a systemic immune response against other tumors in the organism; this has been done from the perspective of a future application of the MNH as a modality for *in situ* vaccination [4,141–143].

We also highlight that, in 2011, Lee et al. [16] investigated the effects of magnetic hyperthermia using magnetic core-shell nanoparticles. The murine tumor model studied was U87MG ($n = 3$ mice), the applied magnetic field was 37.3 kA.m^{-1}, with a frequency of 500 kHz. According to the authors, only 75 μg of $CoFe_2O_4$ – $MnFe_2O_4$ core-shell nanoparticles were injected intratumorally. The mice were followed for only 26 days after treatment, showing complete tumor remission in this period. Despite the quite short time of monitoring, in comparison with the negative control animals (without treatment) and with the positive control animals (treated with the chemotherapy drug doxorubicin), the greater effectiveness of the MNH treatment is clear. The therapeutic potential of magnetic core-shell nanoparticles is really exciting and has been the focus of some other reports in the literature [144].

Since other hyperthermia modalities are already used in clinical applications as a radiation and/or chemo sensitizer [145,146], one can expect interesting results for combined therapies with MNH, which might help the translation to clinic. In fact several interesting multimodal approaches have been proposed, for example, in a recent report Ma et al. (2019) developed a theranostic nanoparticle called Fe_3O_4-Pd Janus (average diameter of the magnetic core equal to 15 nm) with dual-mode magnetic resonance imaging/photoacoustic imaging properties that could be used for both PTT and MNH *in vivo* applications and, simultaneously, a chemodynamic therapy increasing the generation of reactive oxygen species (ROS) in the tumor microenvironment. The murine tumor model studied was 4T1 orthotopic mouse breast cancer (tumor volume of 60 mm^3). The application of MNH (alone) in a first group ($n = 5$) resulted in a small inhibition in the mice tumor growth ratio of 48.6% compared with the control group (non-treated animals). In contrast, by using the combination of MNH + PTT ($\lambda = 808$ nm, $p = 0.5$ W.cm^{-2}) in a second group ($n = 5$) of treated mice,

100% of complete tumor remission was reported (but animals were followed for only 18 days after the combined treatment) [22].

Another smart platform has been developed by Mai et al. for *in situ* heat-triggered drug release mediated by MNH. In this case iron oxide nanocubes (19 nm) surface-coated with a temperature-responsive polymer were synthesized. The polymer undergoes conformational changes for temperatures $\geq$ 41 °C, and are able release previously loaded Doxorubicin content (47 $\mu g_{(DOXO)}$ per 1 $g_{(Fe)}$). The thermo-responsive nanocubes (TR-cubes) have a quite high *in vitro* SLP value (range 157–250 $W{\cdot}g^{-1}$(Fe)) within safe AMF conditions (H = 11 $kA.m^{-1}$ and f = 110 kHz). In this report nude mice bearing solid and subcutaneous tumors of A431 epidermoid carcinoma (80–100 mmn^3) was separated in three groups: a first negative control ($n = 6$) that received only Doxorubicin (injected intravenously) for standard treatment; a second positive control ($n = 6$) where each animal received intratumoral injection of TR-cubes magnetic fluid (0.7 $mg_{(Fe)}$ per animal) for *in vivo* MNH (alone); and a third group ($n = 6$) where each animal received intratumoral injection of Doxorubicin loaded TR-cubes (DOXO-TR-cubes) for combined chemotherapy + MNH (0.7 $mg_{(Fe)}$ per animal). The application of three sessions of 30 min of MNH (alone) in the second group (one treatment per day) produced a better tumoral response than the negative control regarding tumor growth inhibition, but all animals were dead 40 days after nanoparticle injection. Complete tumor remission (confirmed by histopathological analysis) was achieved only with combined therapy in the third group, also submitted to three sessions of 30 min of MNH (applying DOXO-TR-cubes) one treatment per day, but now due to the combined effect of heat and drug release. A survival rate of around 33% is reported for animals followed up to 90 days after nanoparticle injection [23].

Combined therapies are interesting approaches, but are beyond the scope of this review, so only these brief two comments are presented as examples.

Table 2 (below in the text) shows some of the MNH preclinical studies reported in the last two decades:

From the reports in Table 2, it was possible to construct a graph in order to confront the two biological safety criteria adopted in the literature, the Atkinson criterion [24] and the Dutz-Hergt criterion [25,26], against the experimental values of the product (AMF amplitude × frequency).

As mentioned earlier, the Atkinson criterion, based on the eddy current term, states that the value of $Hf \leq 4.85 \times 10^8$ $A.m^{-1}.s^{-1}$ should not be exceeded in order to avoid unwanted tissue injuries. According to this criteria it is clear from Figure 1 that no preclinical study from the literature is satisfactory (as far as we know) which means, in principle, that the experimental conditions that have been studied would not be applicable for human use, since they are predicted to generate a lot of non-localized heat by eddy currents. This is very disappointing, and suggests that several studies had not focused enough on the priority for clinical translation, which is related to improving the heating efficiency of magnetic nanoparticles at low-field condition [147,148]. On the other hand, Dutz and Hergt suggest that this limit can increase by a factor of 10 [25,26]; even so, note that only a few investigations are within the expected safety range of the second clinical limit.

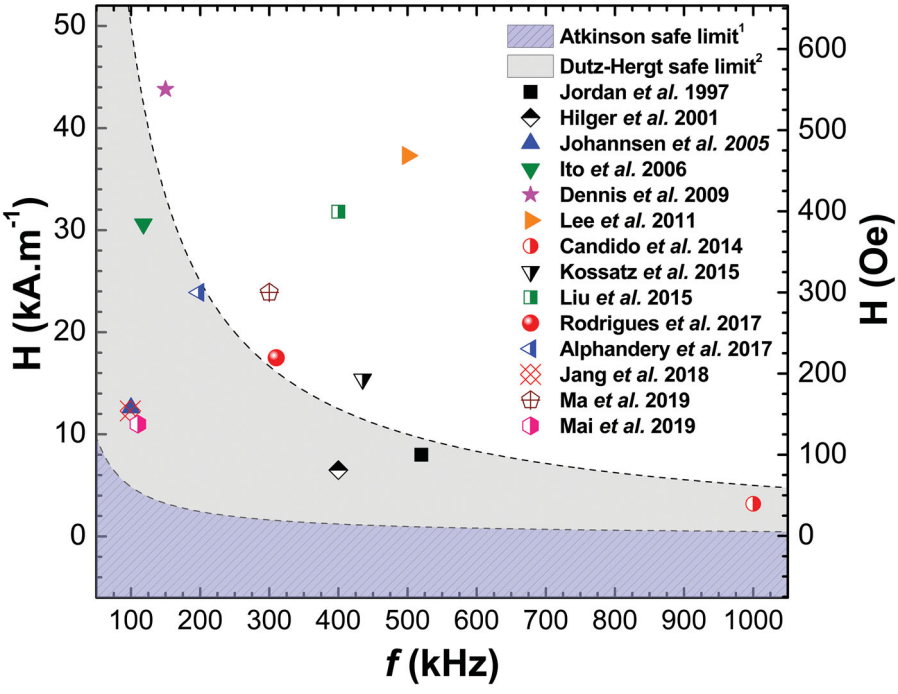

Figure 1. In several preclinical studies reported on the literature, the experimental setups for *in vivo* MNH are out of the clinical safe-limit region (some much more than others): at the graph the dashed and shaded areas delimits, respectively, the Atkinson[1] and Dutz-Hergt[2] thresholds to prevent harmful non-localized heating regime due to eddy currents. The points correspond to the ordered pair of the experimental values for frequency f (in kHz) and amplitude H (in $kA.m^{-1}$ and Oe) of the AMF for the reports presented in Table 2.

Table 2. Preclinical studies that show the effect of MNH (alone) in the treatment of solid tumors.

Preclinical Study	Treated Animals	Solid Tumor Model (Tumor size)	Nanocarrier (magnetic core size)	H[a] [kA.m^{-1}]	f[kHz]	$SLP_{in\ vitro}$	Amount of Injected NP[b]	Tumoral Heating	Days after MNH[c]	Biological Outcome
Jordan et al. 1997 [10]	$n = 13$	C3H mammary carcinoma (120–400 mm^3)	#P6: Fe_3O_4-Dextran (3.1 ± 0.7 nm)	6.8	520	160 W.g$^{-1}_{(NP)}$	10.5 $\mu g_{(Fe)}$.mm$^{-3}_{(tumor)}$	47 ± 1 °C for 30 min	60	Inhibition of tumor growth ration (44% of PR[d])
Hilger et al. 2001 [11]	$n = 10$	MX-1 adenocarcinoma (299 ± 158 mm^3)	Fe_3O_4 (10 nm)	6.5	400	211 W.g$^{-1}_{(NP)}$	(70 ± 30) $\mu g_{(NP)}$.mm$^{-3}_{(tumor)}$	71 ± 8 °C	—	Tumor shrinkage after MNH and CR[e]
Johannsen et al. 2005 [12]	$n = 12$	Dunning R3327 Prostate (740 mm^3)	Fe_3O_4-aminosilan core-shell (15 nm)	12.6	100	160 W.g$^{-1}_{(NP)}$	60 $mg_{(NP)}$.cm$^{-3}_{(tumor)}$	50 °C for 30 min	10	Inhibition of tumor growth ratio (44.1–50.9% of PR)
Ito et al. 2006 [13]	—	B16, MM46, Os515, Vx-7, T-9	Fe_3O_4-Cationic Liposomes (10 nm)	30.6	118	—	—	43–45 °C for 20 min	28	CR (T-9 glioma) + antitumor immune response
Dennis et al. 2009 [14]	$n = 4$	MTG-B mammary (180 ± 40 mm^3)	Fe_3O_4-Dextran (BNF) (~ 50 nm)	43.8	150	81 ± 2 W.g$^{-1}_{(Fe)}$	(4.98 ± 0.03) $mg_{(Fe)}$.cm$^{-3}_{(tumor)}$	40.5–55 °C for 15 min	60	75% of CR
Hou et al. 2009 [15]	$n = 6$	Colorectal (CT26) (D = 0.7 − 1.2 cm)	Magnetic Hydroxyapatite (mHAP) (20–50 nm)	3.8	—	—	160 $mg_{(NP)}$.ml$^{-1}_{(Fluid)}$	45–46 °C for 20 min/day (9 days)	15	100% of CR
Lee et al. 2011 [16]	$n = 3$	U87MG human brain (100 mm^3)	$CoFe_2O_4$-$MnFe_2O_4$ core-shell (15 nm)	37.3	500	2280 W.g$^{-1}_{(NP)}$	0.75 $\mu g_{(NP)}$.mm$^{-3}_{(tumor)}$	—	26	100% of CR
Candido et al. 2014 [17]	$n = 6$	UM-SCC14A oral carcinoma (200 − 250 mm^3)	ϫ-Fe_2O_3 Tripolyphosphate (8 nm)	3.2	1000	—	7×10^{14} Particles.ml$^{-1}_{(Fluid)}$	—	7	100% of CR
Kossatz et al. 2015 [18]	$n = 26$	MDA-MB-231 breast adenocarcinoma (100 − 250 mm^3)	MF66-N6L, MF66-DOX or MF66-N6LDOX (Fe_3O_4 core with 12 ± 3 nm)	15.4	435	500 W.g$^{-1}_{(Fe)}$	2.5 $\mu g_{(Fe)}$.mm$^{-3}_{(tumor)}$	41.7 °C for 60 min/day (2 days)	28	50% of CR: animals with a tumoral reduction to less than 20% of the initial volume
Liu et al. 2015 [19]	$n = 2$	MCF-7 breast cancer (~ 500 mm^3)	Fe_3O_4 ferrimagnetic vortex-domain Nanorings (70 nm)	31.8	400	1500 W.g$^{-1}_{(NP)}$	300 $\mu g_{(NP)}$.cm$^{-3}_{(tumor)}$	44 ± 0.5 °C for 10 min	40	100% of CR
Alphandéry et al. 2017 [20]	$n = 10$	Intracranial U87-Luc GBM (3 − 25 mm^3)	Chains of Magnetosomes (~ 45 nm)	23.9	198	57 ± 6 W.g$^{-1}_{(Fe)}$	1–13 $\mu g_{(Fe)}$.mm$^{-3}_{(tumor)}$	ΔT = 28.5 °C 30 min/day (15 days)	150	40% of CR in the 35th day after MNH (all tumors with 3 mm^3)
Jang et al. 2018 [21]	—	Hep3B subcutaneous (~ 1000 mm^3)	Mg_{013}-γFe2O3 (7 nm ± 10%)	12.3	99	2300–3900 W.g$^{-1}_{(NP)}$	1.15 $mg_{(NP)}$.ml$^{-1}_{(Fluid)}$	50.2 °C for 15 min	14	100% of CR
Ma et al. 2019 [22]	$n = 5$	4T1 orthotopic mouse breast cancer (60 mm^3)	Fe_3O_4-Pd Janus (15 nm)	23.9	300	—	6.0 $\mu g_{(Fe)}$.g$^{-1}_{(tumor)}$	35.6–42 °C for 8 min	18	Inhibition of tumor growth ratio (48.6% of PR)
Mai et al. 2019 [23]	$n = 6$	A431 epidermoid carcinoma (80–100 mm^3)	Iron Oxide Nanocubes (TR-cubes) (19 nm)	11	110	157.2–247 W.g$^{-1}_{(Fe)}$	0.7 $mg_{(Fe)}$ per animal	ΔT = 15 °C 30 min/day (3 days)	~ 35	Inhibition of tumor growth ratio

[a]H-field rms values; [b]In all these studies the amount of nanoparticles (NP) was intratumorally injected; [c]Time period that the animals were followed after MNH treatment; [d]PR: Partial Remission, i.e., re-growth of the local tumor tissue exposed to heat; [e]CR: Complete Remission, i.e., no re-growth of the local tumor tissue exposed to heat;.

Low-field magnetic nano-heaters

MNH therapy involving the intratumoral delivery of MIONP and the external application of AMF to the patient's body can be used to generate localized hyperthermia *via* magnetic hysteresis loss [52,53]. Since 2012, this kind of thermal therapy, in combination with RT, has been approved in Europe for the treatment of human recurrent GBM [52,149], and the feasibility, safety and efficacy of intratumoral injection of aminosilane-coated MIONP was demonstrated in two clinical trials of patients with recurrent GBM in combination with fractionated RT [52,53]. However, this approach has the following limitations: first, a high concentration of MIONP (50–100 $mg_{(Fe)}.g^{-1}$ of tumor) is required for MNH, and this can result in surrounding brain toxicity; second, MIONP are typically delivered by intratumoral stereotactic injection, resulting in leakage and a heterogeneous MIONP distribution that contribute to limited MNH efficacy at the infiltrative tumor margin and off-target heating of the surrounding brain [150,151].

To address some of the current limitations of this thermal therapy modality, not only for GBM treatment but mainly for its widespread application as an elective treatment modality for cancer, the development of better nano-heaters with low toxicity formulations and high specific loss power (SLP) in low-field conditions (i.e., feasible combinations of AMF amplitude and frequency) [148], are eagerly needed in order to explore the real potential of the technique, which in principle might not need to be combined with ionizing radiation.

In a sea of propositions that have popped-up in the last decade, there are some strategies in the material science literature that could be highlighted, as for instance those involving: the control of nanoparticle shape, size and architecture aiming to maximize magnetic energy conversion in heat power (e.g., clustering small magnetic cores forming big nanocarriers); the use of metallic doping species such as Zn, Co or Mn in MIONP, but whose toxicity in the live organism needs to be carefully evaluated; the core-shell structures in which, depending on the nature of the covering layer adsorbed to the magnetic core, can even be used for more than one localized heat generation modality (e.g., MNH plus PTT [22]). About this issue, in Table 3 we summarize and order in a time-line some interesting works related to mono-core and multicore nanocarriers designed in the last 12 years, aiming a better SLP performance for *in vivo* MNH.

The data in Table 3 are only a brief overview of the cited works and, as we can see, to date most of these studies have been betting on the use of magnetite (Fe_3O_4) and maghemite (γ-Fe_2O_3) based magnetic cores (bare or coated with organic or inorganic layers) as nano-heaters for MNH applications. Other materials, such as the manganite perovskite oxides ($La_{1-x}Sr_xMnO_3$), have also been suggested, since their exhibit a wide range of Curie temperatures (T_c) values (up to 90 °C) and can maintain their heat generation capacity (by hysteresis loss mechanism) even after reached the ablative regime ($\geq$48 °C) inside the tumoral mass. For instance, in this kind of material this magnetic property can be tuned by varying Sr-doping levels in the composition [159], and according to the literature this material responds at very low-field conditions. However, a careful toxicity analysis of such material is absent, which might limit its clinical use.

Only four of the reported studies in Table 3 have already been used for *in vivo* applications, namely Dennis et al. [14] (commercial multicore BNF nanoparticles), Rodrigues et al. (cluster of $MnFe_2O_4$ cores coated with DMSA – also multicore nanoparticles) [76], Soleymani et al. ($La_{0.73}Sr_{0.27}MnO_3$ nanoparticles) [159] and Mai et al. (Iron Oxide Nanocubes) [23], with some reporting partial or even complete remissions outcomes in solid murine tumoral models for animals that underwent MNH. In particular, the BNF nanoparticle is probably the most widely tested *in vivo* [14,169,170] nanocarrier of those listed in Table 3, although conclusions from some data should be taken very carefully. For instance, In Dennis et al. Ref. [98], the specific loss power was reported to be 81 $W.g^{-1}_{(Fe)}$, while in Ref. [156] of the same group, the reported value is 550 $W.g^{-1}_{(Fe)}$. The explanation for the difference between them was already addressed in Ref. [152], being related to a collective state. So basically, the lower SLP value is related to mono-core nanoparticles, while the higher SLP values appeared from multicore nanoparticles. Indeed, in Table 3 we report several multicore nanoparticles, some of them named as nanoflowers. This type of nanostructures shows very interesting properties for low-field applications, although the reason for such phenomena is not clear theoretically.

Similarly to Figure 1, the graph in Figure 2 is a comparison of the ordered pair values for frequency *f* (in kHz) and amplitude *H* (in $kA.m^{-1}$ and Oe), for each AMF setup taken from Table 3, in order to check how many of them are within the expected safe range to avoid harm during *in vivo* MNH. Several samples seem to be at least close to the Dutz-Hergt criterion, which suggests that such multicore nanostructures have potential for clinical use. In addition, soft spinel-ferrites-based materials are often associated with high SAR values at low frequency and field conditions and some of the nanomaterials mentioned appear in Table 3 [76,155,162,164,167]. Multicore nanoparticles of such type of materials might also be relevant for clinical applications.

However, one must note a lack of more consistent tests *in vivo* for most of the nano-heaters in Table 3 in order to validate their heat performance in realistic scenarios. So far, several of these studies do not seem to have focused enough on the clinical translation of their outcomes, since no preclinical studies are reported. Achieving the low-field feasible conditions for human applications still seems to be a challenge that needs future research. Nevertheless, paraphrasing Richard Feynman, 'there is [still] plenty of room' for improvements when it comes to the development of low-field nanoheaters realistically suitable for safe clinical applications of MNH. A more complete understanding of the physics of heat generation with such multicore nano-heaters might have a great impact on clinical applications.

Overall, from the reported *in vivo* results in the literature, it is clear that nobody, as far as we know, has so far theoretically correlated the clinical outcome with the intratumoral thermal dose in MNH. In order to achieve this goal, it is of

Table 3. Some mono-core and multicore nano-heaters (from 2008 to 2019), targeted for better SLP performance with *in vivo* MNH.

Study	Material	Type	Core size (obtained by)	Multicore size (obtained by)	H^a [kA.m^{-1}]	f[kHz]	$H \times f$ [A.m^{-1}s^{-1}]	$SLP_{in\ vitro}$	Fluid Volume (concentration)	Temperature rise	Heating time
Dennis C.L. et al., 2008 [152]	γ-Fe_2O_3 (core) Dextran (shell)	Cluster of BNF core-shell nanoparticles (NPs)	44 ± 13 nm (AUC[b]) and 50 nm (HRTEM[c])	92 ± 14 nm (PCS[d])	86	150	1.3×10^{10}	1075 W.g$^{-1}_{(Fe)}$	– (3200 mg$_{(Fe)}$.ml^{-1})	–	–
Lartigue L. et al., 2012 [153]	γ-Fe_2O_3	Cluster of γ-Fe_2O_3 cores forming a NF[e] structure	10.5 nm (XRD[f])	24 nm (HRTEM)	25	520	1.3×10^{10}	~1500 W.g$^{-1}_{(Fe)}$	300 µl (4.8 mg$_{(Fe)}$.ml^{-1})	from 37 °C to ~ 65 °C	~ 28 s
Hugounenq P. et al., 2012 [154]	γ-Fe_2O_3	Cluster of γ-Fe_2O_3 cores forming a NF structure	11 nm (XRD)	42 nm (HRTEM)	11	400	4.4×10^9	500 W.g$^{-1}_{(Fe)}$	300 µl (2.8 mg$_{(Fe)}$.ml^{-1})	–	–
Liu X.L. et al., 2014 [155]	$MnFe_2O_4$	Polymeric nanospheres loaded with $MnFe_2O_4$ NPs	18.0 ± 0.9 nm (HRTEM) 17.03 nm (XRD)	106 nm (DLS)	4	435	1.7×10^9	332 W.g$^{-1}_{(Fe+Mn)}$	1 ml (0.3 mg$_{(Fe+Mn)}$.ml^{-1})	from 30 °C to 45 °C	800 s
Dennis C.L. et al., 2015 [156]	γ-Fe_2O_3 (core) Dextran (shell)	Cluster of BNF core-shell NPs	~ 50 nm (HRTEM)	126 nm (DLS[g])	40	150	6.0×10^9	~550 W.g$^{-1}_{(Fe)}$	1 ml (11 mg$_{(Fe)}$.ml^{-1})	–	30 s
Shubitidze F. et al., 2015 [157]	γ-Fe_2O_3	IONPs[h] with saccharide chains in a NF structure	2–5 nm (HRTEM)	20–40 nm (HRTEM)	~ 35.8	164	5.9×10^9	~190 W.g$^{-1}_{(Fe)}$	1 ml (5 mg$_{(Fe)}$.ml^{-1})	–	–
Das R. et al., 2016 [158]	Ag (core) Fe_3O_4 (shell)	Core-shell (Ag/Fe_3O_4) NPs forming a NF	Core: 45 ± 10 nm (XRD) Shell: 40 nm (XRD)	120 ± 10 nm (HRTEM)	63.66	310	2.0×10^{10}	167 W.g$^{-1}_{(NP)}$	– (2 mg$_{(NP)}$.ml^{-1})	from ~ 22 °C to ~ 50 °C	300 s
Rodrigues H.F. et al., 2017 [76]	$MnFe_2O_4$	Cluster of $MnFe_2O_4$ cores coated with a DMSA	15 ± 3 nm (HRTEM) and 14.1 ± 2.1 nm (XRD)	64.2 nm (DLS)	17.5	301	5.3×10^9	128 W.g$^{-1}_{(NP)}$	90 µl (~ 26 mg$_{(NP)}$.ml^{-1})	from 25 °C to 50 °C	30 s
Soleymani M. et al., 2017 [159]	Mn-perovskite $La_{1-x}Sr_xMnO_3$	Core-Shell NPs $La_{0.73}Sr_{0.27}MnO_3$	54 nm (HRTEM)	Not applicable	2.7	120	3.2×10^8	25.5 W.g$^{-1}_{(NP)}$	1 ml (100 mg$_{(NP)}$.ml^{-1})	from 20 °C to 50 °C	~ 20 s
Hemery G. et al., 2017 [160]	γ-Fe_2O_3	Cluster of γ-Fe_2O_3 PEGylated cores	14.5 ± 3.4 nm (HRTEM)	29.1 ± 4.4 nm (HRTEM)	10	755	7.6×10^9	265 W.g$^{-1}_{(Fe)}$	1 ml (3 mg$_{(Fe)}$.ml^{-1})	from 37 °C to ~ 67 °C	5 s
Gavilan H. et al., 2017 [161]	γ-Fe_2O_3	γ-Fe_2O_3 NPs (coated with Citric Acid) forming a NF	23.7 ± 0.2 nm (XRD)	58 ± 11 nm (HRTEM)	23.8	419	1.0×10^{10}	~440 W.g$^{-1}_{(Fe)}$	–	–	–
Phong P.T. et al., 2017 [162]	$Mn_{0.5}Zn_{0.5}Fe_2O_4$	Nanosized mixed ferrite $Mn_{0.5}Zn_{0.5}Fe_2O_4$	14 nm (XRD) and 15 nm (HRTEM)	Not applicable	6.4	178	1.1×10^9	28.38 W.g$^{-1}_{(NP)}$	1 ml (3 mg$_{(NP)}$.ml^{-1})	from 30 °C to ~ 45 °C	1500s
Bender P. et al., 2018 [163]	γ-Fe_2O_3 and Fe_3O_4	Cluster of IONPs (FeraSpin^{TM}R)	6 nm (HRTEM) and 9 nm (XRD)	18–56 nm (SAXS[i])	7	934	6.5×10^9	226.99 ± 7.32 W.g$^{-1}_{(Fe)}$	– (5 mg$_{(Fe)}$.ml^{-1})	–	–
He S. et al., 2018 [164]	$Zn_xFe_{3-x}O_4$	Core-Shell NPs $Zn_{0.3}Fe_{2.7}O_4$-SiO_2	22 nm (HRTEM)	Not applicable	13	380	4.9×10^9	1010 W.g$^{-1}_{(Fe)}$	– (1 mg$_{(Fe)}$.ml^{-1})	from ~ 20 °C to ~ 46 °C	180 s
Bender P. et al., 2019 [165]	γ-Fe_2O_3	Cluster of γ-Fe_2O_3 cores coated with a dextran	5–15 nm (XRD)	39.0 ± 0.3 nm (HRTEM)	7	934	6.5×10^9	289 W.g$^{-1}_{(Fe)}$	– (5 mg$_{(Fe)}$.ml^{-1})	–	–
Curcio A. et al., 2019 [166]	γ-Fe_2O_3	Core-shell (γ-Fe_2O_3-CuS) IONPs forming a NF	25.5 ± 2.7 nm (HRTEM)	120.4 ± 7.3 nm (HRTEM)	14.35	471	6.8×10^9	~500 W.g$^{-1}_{(Fe)}$	100 µL (~ 2.8 mg$_{(Fe)}$.ml^{-1})	From ~ 25 °C to 55 °C	300 s
Sol-Fernandez S. et al., 2019 [167]	$MnFe_2O_4$	Mn-IONPs coated with DMSA forming a NF	17.0 ± 1.6 nm (HRTEM) and 12 nm (XRD)	67 nm (DLS)	47	96	4.5×10^9	689 W.g$^{-1}_{(Fe+Mn)}$	1 ml (1 mg$_{(Fe+Mn)}$.ml^{-1})	from ~ 22 °C to ~ 35 °C	300 s
Ognjanovic M. et al., 2019 [168]	–	Cluster of IONPs coated with poly(acrylic acid)	13.5 ± 1.2 nm (HRTEM)	24.8 ± 4.4 nm (HRTEM)	15.95	252	4.0×10^9	478 W.g$^{-1}_{(NP)}$	1 ml (5 mg$_{(NP)}$.ml^{-1})	from 25 °C to 55 °C	60 s
Mai et al., 2019 [23]	–	Iron Oxide Nanocubes (TR-cubes)	19 nm (HRTEM)	–	11	110	1.2×10^9	157–247 W.g$^{-1}_{(Fe)}$	100 µL (3 mg$_{(Fe)}$.ml^{-1})	from 25 °C to 55 °C	1800s

(–) The information was not reported by the authors; [a]*H*-field rms values; [b]AUC: Analytical ultracentrifugation; [c]HRTEM: High resolution transmission electron microscopy; [d]PCS: hydrodynamic diameter by Photon Correlation Spectroscopy; [e]NF: Nanoflower, i.e., NPs clustering in a flower-like structure; [f]XRD: Powder x-ray diffraction; [g]DLS: Dynamic light scattering; [h]IONPs: Iron oxide nanoparticles; [i]SAXS: small-angle x-ray scattering.

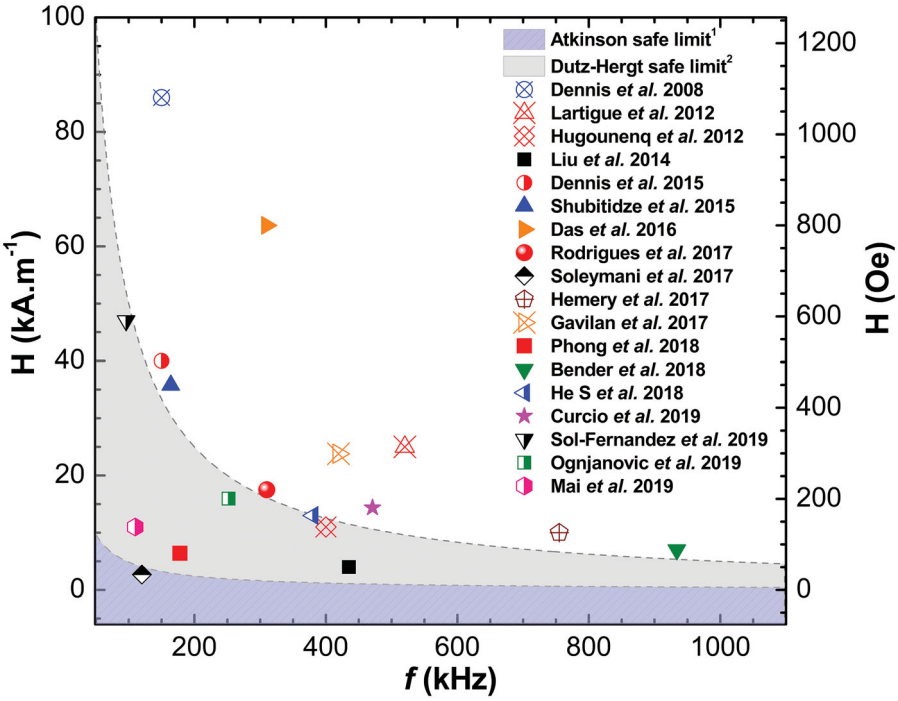

Figure 2. In several *in vitro* studies reported on the literature, the experimental MNH setups are out of the clinical safe-limit region (some much more than others): in the graph the dashed and shaded areas delimit, respectively, the Atkinson[1] and Dutz-Hergt[2] thresholds to prevent harm in human applications (minimizing the off-target heating due to eddy currents). The points correspond to the ordered pair of the experimental values for frequency f (in kHz) and amplitude H (in kA.m^{-1} and Oe) of the AMF for each work presented in Table 3.

fundamental importance to determine, if possible noninvasively, the three-dimensional intratumoral heat deposition. An alternative to achieve this goal is to combine temperature measurements with heat transport numerical simulations. However, this approach for MNH might still be in its infancy, as discussed in the next section. But, this is crucial for the success of MNH since the ability to predict heat delivery during treatment is a great concern for clinical translation. Therefore, it is very important to evaluate treatment planning and correlate, if possible, the therapy with the clinical outcome using computer simulations.

Treatment planning and computer simulations for *in vivo* MNH

Hyperthermia computer simulations are not new, but most groups dealing with MNH mainly focus on the mechanisms of heat generation [7–9,171]. In contrast, realistic *in vivo* numerical simulations are quite rare (see Table 4). The reason might be related to the fact that in the real-life *in vivo* scenario one also deals experimentally with heat monitoring, while theoretically one needs to determine heat transport within the organ of interest during MNH. The solution for this problem can be obtained (at least in murine tumor models) by numerically solving the Pennes' Bioheat Transfer equation, that is given by [178,179]:

$$\rho_n c_n \frac{\partial T_n}{\partial t} = \kappa_n \nabla^2 T_n + \rho_b c_b \omega_{b,n}(T_b - T_n) + \dot{Q}_{met_n} + \dot{Q}_{MNP,n} \quad (7)$$

where ρ_n is the density of the medium [kg.m^{-3}] and n refers to the medium under consideration (e.g., an underwrite (t) to designate tumor tissue or (h) for healthy tissue), ρ_b is the blood density [kg.m^{-3}], c_n is the specific heat of the medium (tissue) [J.kg^{-1}.K^{-1}], κ_n thermal conductivity of the tissue [W.mK^{-1}], c_b is specific heat of the blood [J.kg^{-1}.K^{-1}], $\omega_{b,n}$ is the blood perfusion rate [s^{-1}], T_b is the blood temperature [K], $\dot{Q}_{met_n}$ is the amount of heat generated metabolically per unit volume [W.m^{-3}], $\dot{Q}_{MNP,n}$ is the amount of magnetic nanoparticle heat generated by hysteretic loss per volume unit during MNH [W.m^{-3}].

The Pennes equation is based on the assumption that heat exchange between blood vessels and surrounding tissue occurs mainly through capillary walls (blood vessels with diameters on the order of 0.01 mm), where the blood speed is very slow. The first term on the right side of the Equation (7) is related to the diffusion of heat in the medium (tissue); the second is a convective term due to blood perfusion; the third is a metabolic term due to the high biochemical reactivity of the tumor cells and, finally, the heat generated due to the interaction of the nanoparticles magnetic moments with the external alternating magnetic field. It is assumed that in this model the rate of blood perfusion is homogeneous and isotropic, but temperature dependent [180].

Note that heat generation by hysteresis loss is only one of the parameters ($\dot{Q}_{MNP,n}$) in Equation (7), and obviously is correlated to the three-dimensional localization of the nanoheaters. Therefore, to correctly address the heat transport problem, one also needs to infer the spatial distribution of the magnetic nanoparticles inside the tumor. This increases significantly the complexity of the problem if realistic results are demanded. So, it is not a surprise that many articles in the literature use very simplified and/or idealized

Table 4. Computer simulations for *in vivo* MNH.

Computational Study	Geometric modeling for animal			Thermal dose	MNP concentration	$\dot{Q}_{SIM}$	$\dot{Q}_{EXP}$	SLP_{SIM}	SLP_{Exp}	H^a	f	Maximum temperature
	Body	Tumor	MNP[b] distribution		[mg.ml^{-1}]	[W.m^{-3}]	[W.m^{-3}]	[W.g^{-1}]	[W.g^{-1}]	[KA.m^{-1}]	[KHz]	[°C]
Pavel et al. 2008 [172]	Cube	Spherical	Spherical	No	10	6×10^9	–	6×10^5	–	14.5	170	42.5
Pavel et al. 2009 [173,174]	No	Spherical	spherical	No	10–10.5	$(6.8–7.5) \times 10^9$	–	–	–	7	200	–
Lebrun et al. 2013 [55]	Parallelepiped	Micro-CT	Pixel dependent	CEM43	–	$1.5 \times 10^4 - 2.9 \times 10^6$	9.8×10^5	–	–	–	190	55
Attaluri et al. 2015 [39]	Spherical shell	Spherical	Spherical	CEM43	–	4.6×10^5	–	–	–	24	155	–
Lebrun et al. 2016 [56]	Modeled from a mouse obtained from a Micro-CT	Micro-CT	Pixel dependent	Ω	–	–	–	–	–	–		–
Pearce et al. 2017 [175]	Box	Ellipsoidal	Spherical	CEM43	1.25	9×10^9	1×10^6	–	–	32.5	162	57
Rodrigues H.F. et al., 2017 [76]	Ellipsoidal	Ellipsoidal	Spherical	No	26	3.9×10^6	3.3×10^6	150	128	17.5	310	50
Li et al. 2019 [176]	Cylindrical	Spherical	Spherical	CEM43	5	–	–	–	–	5	100	43
Jin et al. 2019 [177]	Spherical shell	Spherical	Spherical	Ω	–	Gaussian distribution	–	–	–	–	300	54.5

The dash (–) means that the information/quantity was not specified/reported by the authors in the paper; [a]*H*-field rms values; [b]MNP: magnetic nanoparticle.

nanoparticle distribution and tumor geometries. In fact, few studies with *in vivo* MNH simulations can be found in the literature, and we summarized some of them in Table 4.

Pavel et al. [172–174] were one of the first to present a MNH computer simulation. Besides not making comparison with experimental data, they used a very high magneto-thermal efficiency value ($\sim 10^5$ W.g^{-1}), which is not consistent with actual experimental data – in this sense, it should also be noted the very high hysteretic loss power value used by Pearce et al. [175]. Also, most of the simulations in the literature, including ours [76], were performed without an adequate three-dimensional reconstruction of the 'object' under study, modeling the 'object' by approximations to simple geometries, such as: cubes, spheres, ellipsoids, cylinders, etc., that do not match reality. For example, in the work of Lebrun et al. [55], the body of the mouse, as a whole, was considered to be a cobblestone, while in our previous work we considered an ellipsoid [76].

So far, distinct strategies to localize the magnetic nano-heaters in the tumor have been suggested but, for instance, LeBrun et al. [56] found from high-resolution micro-CT images that nanoparticles do not always remain confined to a spherical region close to the injection site. Indeed, several authors have shown that the nanoparticles distribute non-homogeneously inside the tumor after the particle injection [57,61,63,181,182].

In this context, the development of more suitable theoretical models able to predict (or refute) the required conditions that the heating regime should achieve (*in vivo*) in order to promote lethal thermal damage of the target tissues, is a mathematical challenge that could be addressed by: (i) first, an accurate description of the spatial distribution of the nano-heaters (after injected within the tumor); (ii) second, reconstructing the realistic geometries where Equation (7) must be solved (i.e., the tumor volume in all its complexity and off-target surrounding structures, including the animal's body if surface temperature measurements are important); iii) third, segmenting the target region and assigning thermal properties to each segment (e.g., tissue density, thermal conductivity, specific heat, metabolic heat power, etc.); and, then to take in account specific non-linear modeling for the tumor blood perfusion rate, since this parameter depends on temperature.

Of all the recently published articles, the one closest to a realistic simulation was the one published by LeBrun et al. in 2016 [56]. In this study, the authors were more careful about the description of the animal's geometry, the tumor, the heat sources and the boundary conditions that involve the computer simulation, such as the temperature-dependent perfusion rate, with a model adopted from Lang [183]. The authors developed an algorithm, in Matlab, capable of three-dimensionally reconstructing the tumor using DICOM image data extracted from Micro-CT. In addition, they propose to use the increase in contrast in Micro-CT, a consequence of the nanoparticle distribution, to locate the heat centers (magnetic nanoparticles), from which they also build a pixel-dependent heat source. However, the model of the animal's body is not identical to the animal submitted for treatment

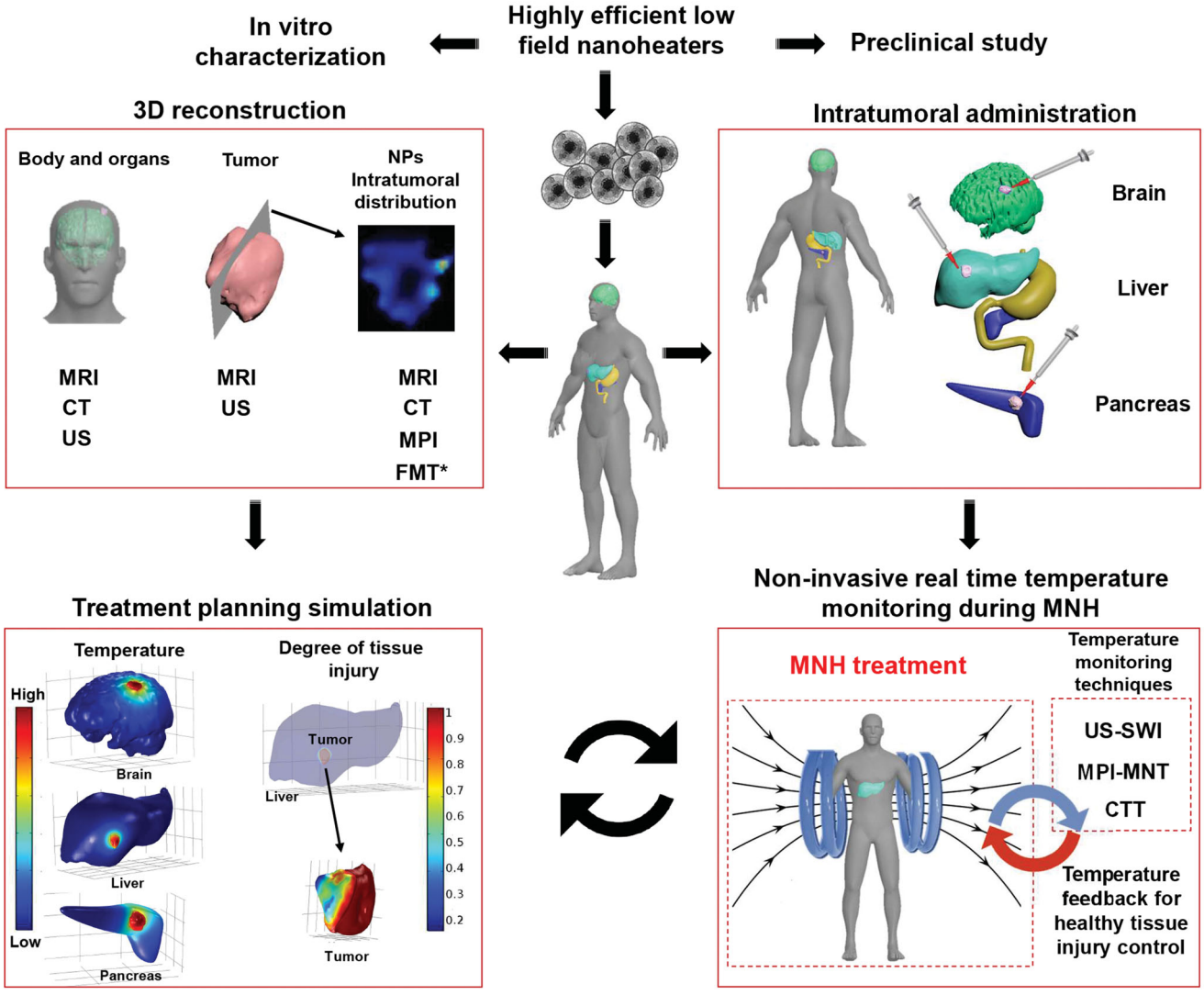

Figure 3. *In vivo* MNH treatment planning algorithm. MRI – Magnetic Resonance Imaging, CT – Computed Tomography, US – Ultrasound, US-SW – Shear wave ultrasound, MPI – Magnetic Particle Imaging, FMT - Fluorescence Molecular Tomography, * Technique useful only for preclinical studies.

by MNH. The tumor, although it is reconstructed from Micro-CT images, has low resolution, as it is reconstructed from few slices. In addition, if one decides to monitor heat deposition using surface temperature measurements with a thermal camera, a very negative impact on predicting the thermal dose can occur due to inadequate animal body geometry.

Overall, once a reliable methodology has been established which indicates that a given computer simulation represents the animal's MNH therapy, it will be possible to predict the temperature profile three-dimensionally for the target tissues (and the surrounding boundary) through numerical calculations, i.e., the intratumoral thermal dose. However, to verify if this theoretically calculated intratumoral dose adequately describes the treatment, a comparison with the clinical situation needs to be made. One approach that is being developed in our research group [89] consists of analyzing histological sections from the necrotic regions of the tumor, resultant from irreversible thermal damages after being subjected to MNH, and comparing these with computer simulations. To ensure good reliability between our computational modeling and the experimental outcomes, we address this problem by combining several techniques. First, photogrammetry is used to obtain the exact shape of the animal's body submitted to the MNH procedure, and since we study subcutaneous tumors, the skin surface thermometry is quite relevant. Second, the 3D geometry of the tumor is reconstructed from two-dimensional ultrasound images by a technique known as freehand 3D ultrasound reconstruction [184]. Finally, to extract information about the location of the nano-heaters, we developed a multifunctional nanocarrier that contains fluorescent tracers in the near infrared, which surface-coat Mn-doped iron oxide-based nanoparticles, so that their location within the tumor can be extracted using the fluorescence molecular tomography (FMT) technique [125,185].

Thereafter, by the fusion of these three complex geometries (body surface, tumor volume and nano-heaters location) it is possible to build a more realistic model (using the commercial software COMSOL Multiphysics) and solve the

bioheat equation (Equation (7)) *via* the Finite Element Method, obtaining the temporal evolution of the intratumoral temperature for each voxel. Then, applying the Equation (6) (also for each voxel) in order to convert this 3D-temperature mapping into an equivalent volume of thermal damage $\Omega(r,t)$ values, we can finally calculate the correspondent three-dimensional degree of tissue injury in order to predict the volumetric fraction of the heated tumor that could be (or not) irreversibly thermally damaged [89].

The following flowchart (Figure 3) summarizes the main steps of general treatment planning for *in vivo* MNH, starting from the synthesis of low-field MIONP and its *in vitro* characterization, passing by the obtention of more realistic and personalized geometric models for the patient's organs, the tumor volume, and the nano-heaters 3D intratumoral location. All of this is necessary in order to calculate numerically the desired temperature increase in the target tissues, recognizing the need for more accurate predictions of the patient's response to thermal therapy. A list of techniques to achieve this goal is also schematized. In addition, we included a chart for noninvasive real time temperature monitoring during MNH that serves as a feedback to control the tissue thermal dose, as well as to correct the simulation predictions, which we expect to orient clinicians in the future, in real-time, during the treatment. Thermometric techniques that have potential to be used together with MNH are also shown:

The success of the treatment planning simulation might have a great clinical impact, since it could indicate why in some cases tumor recurrence may occur. Nevertheless, it might be fair to mention that only a few groups are actually developing strategies to combine MNH *in vivo* studies with 'realistic-like' computer simulations with the aim to predict the clinical outcome or noninvasively determine the three-dimensional intratumoral thermal dose. It should be highlighted that in some works this kind of approach is also linked to the challenge of improving heat-induced immunological stimulations [4,13,141], and therefore is expected to impact heat-triggered cancer immunotherapy.

From all previous comments, it is clear that noninvasively extracting the intratumoral thermal dose for MNH is a very challenging task, and even though it is called realistic, a computer simulation will never be able to accurately reproduce an *in vivo* experiment, because the number of random variables and uncertainties is large. Nevertheless, if the approximations are good, one expects to be able to explain the clinical outcome due to the therapeutic procedure. Also, one expects that during MNH treatment, by noninvasive real time temperature monitoring with some clinical technique (see Figure 3), corrections on the simulations could be envisioned during treatment, affecting clinical decisions focused on better thermal dose control.

Final considerations and future directions

To date, certain challenges remain in the current approaches for clinical applications of MNH [54], limiting its effective use, since MNH is not yet part of the clinical standard of care for cancer treatment. Among these is the need for the development of nano-heaters able to deliver (*in vivo*) a high SLP response at AMF low-field conditions (focusing on the clinical safety criteria), the need for more accurate thermometry within the tumoral mass and precise tumor heating (limiting healthy tissue off-target) and, finally, more realistic computational modeling for better MNH treatment planning.

As previously mentioned, and going a bit farther with regard to the problem of real-time monitoring of the intratumoral heat deposit compatible with *in vivo* MNH setups, LNT may offer a possible alternative to extract temperatures inside the animal, but only up to around 1 cm [186]. However, a limitation remains, since it is not easy to infer precisely at what position and volume of interest the temperatures are being measured, in some cases because of scattering due to the biological media. But, although this technology is very interesting, it still can have a negative impact on the ability to predict thermal deposition if the tumors are not very small. Also, in this case, the magnetic nano-heaters have to be combined with luminescent nanothermometers, which increase the complexity of the nanocarrier [79]. Photoacoustic thermometry is also an alternative showing temporal resolution for *in vivo* applications, but again is depth-restricted [187].

One might think that another option could be to explore low-field MRI scanners, and consequently use the gold-standard 3D MRI thermometry [188]. But the technology here is limited to *DC* fields within the range of 0.25–1 T, that unfortunately still has a very high static magnetic field able to inhibit the MIONPs heat generation under AMF excitation [2,32]. Moreover, even if MRI thermometry was possible, it might be difficult to implement this methodology using MIONPs because the vicinity is strongly influenced by the magnetic material, which can feel significant variations in the MRI signals, thus inhibiting the thermometry implementation with the PRF method [44].

An alternative way to solve this problem is to use strong magnetic field gradients, as extensively explored with the MPI technology [189,190]. In this case one promotes a field free region (FFR) that allows the excitation of nanoparticles by AMF and promote heat generation within the ROI. Indeed, recently the development of a dual MPI-MNH system was demonstrated, where MPI excites the nanoparticles at *AC* induction fields of 20 kHz, while MNH is tuned to generate heat at 354 kHz [80,191]. Both *in vitro* and *in vivo* studies of the MPI-MNH system were able to demonstrate heat generation in specific ROIs. The heat delivery as function of the distance from FFR (at 354 kHz) was analyzed using a theoretical approach that assumes a magnetization equation due to particle rotation (Brownian relaxation) [86]. From this analysis, the authors extract the value of heating efficiency (SAR/SLP) in a particular position in space. However, the limitation of this methodology, as will become clear below, is that at MNH frequencies ranging from 100 to 500 kHz the rotation does not play any role in heat generation, so it might not reveal adequately heat deposition. Also, the method does not directly obtain the information about the temperature, so thermal dose estimations might be limited.

On the other hand, the magnetic response signal of the nanoparticles measured as a result of the AMF excitation might carry important information for thermometry. This is expected, not only because the particle magnetization $M(T)$ is temperature dependent (usually follows Bloch's law: $M(T) = M(T_0)[1-(\frac{T}{T_c})^{\frac{3}{2}}]$, where T_c is the critical temperature), but also due to the strong effect on magnetization relaxation processes. The Brownian relaxation is influenced through temperature dependence of the viscosity, while for Néel relaxation temperature appears in the exponential term, not forgetting that even the anisotropy of the material is temperature dependent. This might be described by the Zener-Callen model, which relates the magnetic anisotropy temperature dependence with the magnetization and the symmetry of anisotropy [147]. Indeed, the MNT technique was suggested some time ago, and relies on taking advantage of the temperature dependence of the harmonic signals, commonly obtained using MPI technology [189]. Moreover, it was suggested to use the ratio of the 5th to the 3rd harmonic of the magnetization to extract the temperature [81], which is obtained from the Fourier transform of the time dependence magnetization response after ac excitation. Here again it is crucial to focus on the frequency range being monitored.

Magnetic particle spectroscopy, that monitors the harmonic signals at 20 kHz, reveals a strong dependence of the signal upon particle-particle and particle-matrix interaction [87]. Immobilizing the nanoparticles strongly affects the harmonic signals, indicating the importance of Brownian relaxation at this frequency range. This is consistent with the analysis of the hydrodynamic radii of multicore nanostructures that, in the range of 50–100 nm, predicts Brownian relaxation in the frequency range lower than 20 kHz, as experimentally found by *AC* susceptibility measurements [192] or estimated theoretically using linear response theory [148]. On the other hand, Bender et al. clearly demonstrated that at typical magnetic hyperthermia frequencies (100–500 kHz) the magnetic response of multicore nanoparticles is governed by intrinsic magnetic relaxation, i.e., by Néel-like relaxation [163,192]. Similar conclusions were obtained by others [156].

In general, one can conclude that the nonlinear magnetization response is related to collective relaxation, but our understanding of this mechanism is still in its infancy. Therefore, it might be fair to mention that our ability to perform magnetic nanothermometry might depend strongly on improving our knowledge of the collective behavior in the next few years, otherwise this thermometry approach might not achieve success. In addition, the field-gradient technology used in MPI has not been translated for human use as yet, although some authors are starting to address this issue [193]. This is eagerly needed and could have a huge impact in clinical translation of MNH.

Moreover, even if the MPI-MNH system is developed for human use in the near future, one expects the price of this technology, at least in the beginning, to be as high as MRI. This is competitive, but there is a low-cost technology that so far has not been adequately applied to MNH, namely ultrasound thermometry (UST). UST has been a topic of interest for a quite long time [1], but its use for thermal medicine applications is curiously not as high as it could be. One possible reason for that is that most thermometry applications appear for ablation therapies, while UST had bet a lot on thermal strain imaging that is known to be applicable at temperatures lower than 50 degrees Celsius. Recently, it was demonstrated in phantom studies that USTSI can be used for real-time temperature monitoring during MNH [77]. However, this approach has significant challenges to be overcome due to animal motion (because of the patient's breathing movements) [194]. Anyway, UST can get benefit from shear wave thermometry, which is less sensitive to respiration and valid in a considerable temperature range [78]. So, we strongly recommend that the scientists in the MNH field interact with ultrasound medical physicists (and engineers) with the objective to develop a low-cost, good accuracy and noninvasive system for *in vivo* real-time temperature monitoring during MNH treatment.

Further, there is a clinical technology that is rising again, namely computed tomography based thermometry (CTT) [82,83]. CTT was suggested several decades ago, but might become a reality now because of innovative filters and new data reconstruction techniques [82]. The challenge of low-dose radiation might be achieved using dual energy imaging systems. However, the proof-of-concept that CTT can be combined with MNH has not been established. This could be an interesting area of research for the future, since CT can also be used to determine the magnetic nanoparticle 3D location, and therefore extract important parameters for realistic treatment planning simulations during MNH.

In conclusion, so far, MNH has been approved only for the clinical treatment of brain tumors together with RT. Ten years have passed since approval and the technology has not expanded yet to other types of tumors (although there is a clinical study underway for prostate cancer treatment). In our opinion, the failure for introducing new clinical applications might be related to the absence of applying noninvasive thermometry in MNH. In this review, we discussed some limitations of this technology and tried to point some future directions. Indeed, we expect a great impact on clinical translation of Magnetic Nanoparticle Hyperthermia if at least one of the technologies mentioned here, namely the ultrasound-based, computed tomography-based or the magnetic nanoparticle-based thermometry, are implemented for *in vivo* applications. This, together with the development of more efficient low-field magnetic nano-heaters and also realistic-like MNH computer simulations for treatment planning could result in a broad range of clinical applications. One expects single therapeutic applications that could span not only from heat-alone treatment applications (ablation technologies) and more importantly, heat-triggered drug release strategies at very well localized regions in the body, to highly efficient heat-induced immunotherapy strategies that should benefit from three-dimensional heat dose control.

Disclosure statement

No potential conflict of interest was reported by the author(s).

Funding

The authors acknowledge the financial support from the following Brazilian agencies: CNPq [Grant No. 310230/2017-9], CAPES, FAPEG [Grant No. 201710267000511].

ORCID

Harley F. Rodrigues http://orcid.org/0000-0001-6991-9670
Andris F. Bakuzis http://orcid.org/0000-0003-3366-106X

References

[1] Moros E. Physics of thermal therapy fundamentals and clinical applications. Boca Raton (FL): CRC/Taylor & Francis; 2013.
[2] Jordan A, Wust P, Fahling H, et al. Inductive heating of ferrimagnetic particles and magnetic fluids: physical evaluation of their potential for hyperthermia. Int J Hyperthermia. 1993;9(1):51–68.
[3] Rastinehad AR, Anastos H, Wajswol E, et al. Gold nanoshell-localized photothermal ablation of prostate tumors in a clinical pilot device study. Proc Natl Acad Sci USA. 2019;116(37):18590–18596.
[4] Toraya-Brown S, Sheen MR, Zhang P, et al. Local hyperthermia treatment of tumors induces CD8(+) T cell-mediated resistance against distal and secondary tumors. Nanomedicine. 2014;10(6):1273–1285.
[5] Bertotti G. Hysteresis in magnetism: for physicists, materials scientists, and engineers. San Diego (CA): Academic Press; 1998.
[6] Rosensweig RE. Heating magnetic fluid with alternating magnetic field. J Magn Magn Mater. 2002;252:370–374.
[7] Verde EL, Landi GT, Gomes JA, et al. Magnetic hyperthermia investigation of cobalt ferrite nanoparticles: comparison between experiment, linear response theory, and dynamic hysteresis simulations. J Appl Phys. 2012;111:123902.
[8] Carrey J, Mehdaoui B, Respaud M. Simple models for dynamic hysteresis loop calculations of magnetic single-domain nanoparticles: application to magnetic hyperthermia optimization. J Appl Phys. 2011;109(8):083921.
[9] Verde EL, Landi GT, Carrião MS, et al. Field dependent transition to the non-linear regime in magnetic hyperthermia experiments: comparison between maghemite, copper, zinc, nickel and cobalt ferrite nanoparticles of similar sizes. AIP Adv. 2012;2:032120.
[10] Jordan A, Scholz R, Wust P, et al. Effects of magnetic fluid hyperthermia (MFH) on C3H mammary carcinoma in vivo. Int J Hyperth. 1997;13(6):587–605.
[11] Hilger I, Andrä W, Hergt R, et al. Electromagnetic heating of breast tumors in interventional radiology: in vitro and in vivo studies in human cadavers and mice. Radiology. 2001;218(2):570–575.
[12] Johannsen M, Thiesen B, Jordan A, et al. Magnetic fluid hyperthermia (MFH)reduces prostate cancer growth in the orthotopic Dunning R3327 rat model. Prostate. 2005;64(3):283–292.
[13] Ito A, Honda H, Kobayashi T. Cancer immunotherapy based on intracellular hyperthermia using magnetite nanoparticles: a novel concept of "heat-controlled necrosis" with heat shock protein expression. Cancer Immunol Immunother. 2006;55(3):320–328.
[14] Dennis CL, Jackson AJ, Borchers JA, et al. Nearly complete regression of tumors via collective behavior of magnetic nanoparticles in hyperthermia. Nanotechnology. 2009;20(39):395103.
[15] Hou C-H, Hou S-M, Hsueh Y-S, et al. The in vivo performance of biomagnetic hydroxyapatite nanoparticles in cancer hyperthermia therapy. Biomaterials. 2009;30(23–24):3956–3960.
[16] Lee J-H, Jang J, Choi J, et al. Exchange-coupled magnetic nanoparticles for efficient heat induction. Nat Nanotechnol. 2011;6(7):418–422.
[17] Candido N, Calmon M, Taboga S, et al. High efficacy in hyperthermia-associated with polyphosphate magnetic nanoparticles for oral cancer treatment. J Nanomed Nanotechnol. 2014;5:206.
[18] Kossatz S, Grandke J, Couleaud P, et al. Efficient treatment of breast cancer xenografts with multifunctionalized iron oxide nanoparticles combining magnetic hyperthermia and anti-cancer drug delivery. Breast Cancer Res. 2015;17:66.
[19] Liu XL, Yang Y, Ng CT, Zhao LY, et al. Magnetic vortex nanorings: a new class of hyperthermia agent for highly efficient in vivo regression of tumors. Adv Mater Weinheim. 2015;27(11):1939–1944.
[20] Alphandéry E, Idbaih A, Adam C, et al. Chains of magnetosomes with controlled endotoxin release and partial tumor occupation induce full destruction of intracranial U87-Luc glioma in mice under the application of an alternating magnetic field. J Control Release. 2017;262:259–272.
[21] Jang J, Lee J, Seon J, et al. Giant magnetic heat induction of magnesium-doped γ-Fe_2O_3 superparamagnetic nanoparticles for completely killing tumors. Adv Mater. 2018;30(6):1704362.
[22] Ma X, Wang Y, Liu X-L, et al. Fe_3O_4–Pd Janus nanoparticles with amplified dual-mode hyperthermia and enhanced ROS generation for breast cancer treatment. Nanoscale Horiz. 2019;4(6):1450–1459.
[23] Mai BT, Balakrishnan PB, Barthel MJ, et al. Thermoresponsive iron oxide nanocubes for an effective clinical translation of magnetic hyperthermia and heat-mediated chemotherapy. ACS Appl Mater Interfaces. 2019;11(6):5727–5739.
[24] Atkinson WJ, Brezovich IA, Chakraborty DP. Usable frequencies in hyperthermia with thermal seeds. IEEE Trans Biomed Eng. 1984;31(1):70–75.
[25] Dutz S, Hergt R. Magnetic nanoparticle heating and heat transfer on a microscale: Basic principles, realities and physical limitations of hyperthermia for tumour therapy. Int J Hyperthermia. 2013;29(8):790–800.
[26] Dutz S, Hergt R. Magnetic particle hyperthermia-a promising tumour therapy? Nanotechnology. 2014;25(45):452001.
[27] Wust P, Hildebrandt B, Sreenivasa G, et al. Hyperthermia in combined treatment of cancer. Lancet Oncol. 2002;3(8):487–497.
[28] van den Tempel N, Horsman MR, Kanaar R. Improving efficacy of hyperthermia in oncology by exploiting biological mechanisms. Int J Hyperthermia. 2016;32(4):446–454.
[29] Bull JMC. A review of immune therapy in cancer and a question: can thermal therapy increase tumor response? Int J Hyperthermia. 2018;34(6):840–852.
[30] Sweeney EE, Cano-Mejia J, Fernandes R. Photothermal therapy generates a thermal window of immunogenic cell death in neuroblastoma. Small. 2018;14(20):e1800678.
[31] Hirsch LR, Stafford RJ, Bankson JA, et al. Nanoshell-mediated near-infrared thermal therapy of tumors under magnetic resonance guidance. Proc Natl Acad Sci USA. 2003;100(23):13549–13554.
[32] Mehdaoui B, Carrey J, Stadler M, et al. Influence of a transverse static magnetic field on the magnetic hyperthermia properties and high-frequency hysteresis loops of ferromagnetic FeCo nanoparticles. Appl Phys Lett. 2012;100(5):052403.
[33] MagForce USA, Inc. MagForce announces enrollment of first patient in its pivotal, three-stage, single-arm study of focal ablation of prostate cancer with nanotherm therapy. n.d. [cited 2020 April 10]. https://magforce.com.
[34] Hilger I. *In vivo* applications of magnetic nanoparticle hyperthermia. Int J Hyperthermia. 2013;29(8):828–834.
[35] Vorotnikova E, Ivkov R, Foreman A, et al. The magnitude and time-dependence of the apoptotic response of normal and malignant cells subjected to ionizing radiation versus hyperthermia. Int J Radiat Biol. 2006;82(8):549–559.
[36] Duval KEA, Vernice NA, Wagner RJ, et al. Immunogenetic effects of low dose (CEM43 30) magnetic nanoparticle hyperthermia and radiation in melanoma cells. Int J Hyperthermia. 2019;36(sup1):37–46.

[37] Petryk AA, Giustini AJ, Gottesman RE, et al. Magnetic nanoparticle hyperthermia enhancement of cisplatin chemotherapy cancer treatment. Int J Hyperthermia. 2013;29(8):845–851.
[38] Johannsen M, Thiesen B, Wust P, et al. Magnetic nanoparticle hyperthermia for prostate cancer. Int J Hyperthermia. 2010;26(8): 790–795.
[39] Attaluri A, Kandala SK, Wabler M, et al. Magnetic nanoparticle hyperthermia enhances radiation therapy: a study in mouse models of human prostate cancer. Int J Hyperthermia. 2015; 31(4):359–374.
[40] Oei AL, Korangath P, Mulka K, et al. Enhancing the abscopal effect of radiation and immune checkpoint inhibitor therapies with magnetic nanoparticle hyperthermia in a model of metastatic breast cancer. Int J Hyperthermia. 2019;36(sup1):47–63.
[41] Rieke V, Butts Pauly K. MR thermometry. J Magn Reson Imaging. 2008;27(2):376–390.
[42] Carter DL, MacFall JR, Clegg ST, et al. Magnetic resonance thermometry during hyperthermia for human high-grade sarcoma. Int J Radiat Oncol Biol Phys. 1998;40(4):815–822.
[43] Wiekhorst F, Trahms L. Use of magnetic nanoparticles in biomedical applications. In: Van de Voorde M, Fermon C, editors. Nanomagnetism: applications and perspectives. Weinheim (Germany): Wiley-VCH Verlag GmbH & Co. KGaA; 2017. p. 137–164.
[44] Stephen ZR, Kievit FM, Zhang M. Magnetite nanoparticles for medical MR imaging. Mater Today (Kidlington). 2011;14(7–8): 330–338.(11)70163-8.
[45] Hilger I, Kaiser WA. Iron oxide-based nanostructures for MRI and magnetic hyperthermia. Nanomedicine (Lond). 2012;7(9): 1443–1459.
[46] Ferrari M. Cancer nanotechnology: opportunities and challenges. Nat Rev Cancer. 2005;5(3):161–171.
[47] Wickline SA, Neubauer AM, Winter PM, et al. Molecular imaging and therapy of atherosclerosis with targeted nanoparticles. J Magn Reson Imaging. 2007;25(4):667–680.
[48] Harisinghani MG, Barentsz J, Hahn PF, et al. Noninvasive detection of clinically occult lymph-node metastases in prostate cancer. N Engl J Med. 2003;348(25):2491–2499.
[49] Roberts TPL, Chuang N, Roberts HC. Neuroimaging: do we really need new contrast agents for MRI? Eur J Radiol. 2000;34(3): 166–178.
[50] Paysen H, Loewa N, Weber K, et al. Imaging and quantification of magnetic nanoparticles: Comparison of magnetic resonance imaging and magnetic particle imaging. J Magn Magn Mater. 2019;475:382–388.
[51] Gneveckow U, Jordan A, Scholz R, et al. Description and characterization of the novel hyperthermia- and thermoablation-system MFH 300F for clinical magnetic fluid hyperthermia . Med Phys. 2004;31(6):1444–1451.
[52] Maier-Hauff K, Ulrich F, Nestler D, et al. Efficacy and safety of intratumoral thermotherapy using magnetic iron-oxide nanoparticles combined with external beam radiotherapy on patients with recurrent glioblastoma multiforme. J Neurooncol. 2011; 103(2):317–324.
[53] Maier-Hauff K, Rothe R, Scholz R, et al. Intracranial thermotherapy using magnetic nanoparticles combined with external beam radiotherapy: results of a feasibility study on patients with glioblastoma multiforme. J Neurooncol. 2007;81(1):53–60.
[54] Mahmoudi K, Bouras A, Bozec D, et al. Magnetic hyperthermia therapy for the treatment of glioblastoma: a review of the therapy's history, efficacy and application in humans. Int J Hyperthermia. 2018;34(8):1316–1328.
[55] LeBrun A, Manuchehrabadi N, Attaluri A, et al. MicroCT image-generated tumour geometry and SAR distribution for tumour temperature elevation simulations in magnetic nanoparticle hyperthermia. Int J Hyperthermia. 2013;29(8):730–738.
[56] LeBrun A, Ma R, Zhu L. MicroCT image based simulation to design heating protocols in magnetic nanoparticle hyperthermia for cancer treatment. J Therm Biol. 2016;62(Pt B):129–137.
[57] Attaluri A, Ma R, Qiu Y, et al. Nanoparticle distribution and temperature elevations in prostatic tumours in mice during magnetic nanoparticle hyperthermia. Int J Hyperthermia. 2011;27(5): 491–502.
[58] Attaluri A, Ma R, Zhu L. Using MicroCT imaging technique to quantify heat generation distribution induced by magnetic nanoparticles for cancer treatments. J Heat Transf. 2010;133: 011003–011003.
[59] Rhoon G. v. Is CEM43 still a relevant thermal dose parameter for hyperthermia treatment monitoring? Int J Hyperthermia. 2016; 32:50–62.
[60] Wilhelm S, Tavares AJ, Dai Q, et al. Analysis of nanoparticle delivery to tumours. Nat Rev Mater. 2016;1(5):16014.
[61] LeBrun A, Joglekar T, Bieberich C, et al. Identification of infusion strategy for achieving repeatable nanoparticle distribution and quantification of thermal dosage using micro-CT Hounsfield unit in magnetic nanoparticle hyperthermia. Int J Hyperthermia. 2016;32(2):132–143.
[62] Jordan A, Scholz R, Wust P, et al. Magnetic fluid hyperthermia (MFH): Cancer treatment with AC magnetic field induced excitation of biocompatible superparamagnetic nanoparticles. J Magn Magn Mater. 1999;201:413–419.
[63] Rodrigues HF, Mello FM, Branquinho LC, Zufelato N, et al. Real-time infrared thermography detection of magnetic nanoparticle hyperthermia in a murine model under a non-uniform field configuration. Int J Hyperthermia. 2013;29(8):752–767.
[64] Ma M, Chen H, Chen Y, et al. Au capped magnetic core/mesoporous silica shell nanoparticles for combined photothermo-/chemo-therapy and multimodal imaging. Biomaterials. 2012; 33(3):989–998.
[65] Di Corato R, Béalle G, Kolosnjaj-Tabi J, et al. Combining magnetic hyperthermia and photodynamic therapy for tumor ablation with photoresponsive magnetic liposomes. ACS Nano. 2015;9(3):2904–2916.
[66] Espinosa A, Di Corato R, Kolosnjaj-Tabi J, et al. Duality of iron oxide nanoparticles in cancer therapy: amplification of heating efficiency by magnetic hyperthermia and photothermal bimodal treatment. ACS Nano. 2016;10(2):2436–2446.
[67] Chanmugam A, Hatwar R, Herman C. Thermal analysis of cancerous breast model. Int Mech Eng Congress Expo. 2012;2012: 134–143.
[68] Bhargava A, Chanmugam A, Herman C. Heat transfer model for deep tissue injury: a step towards an early thermographic diagnostic capability. Diagn Pathol. 2014;9:36.
[69] Hatwar R, Herman C. Inverse method for quantitative characterisation of breast tumours from surface temperature data. Int J Hyperthermia. 2017;33(7):741–757.
[70] Zhou Y, Herman C. Optimization of skin cooling by computational modeling for early thermographic detection of breast cancer. Int J Heat Mass Transf. 2018;126:864–876.
[71] Herman C. The role of dynamic infrared imaging in melanoma diagnosis. Expert Rev Dermatol. 2013;8(2):177–184.
[72] Kateb B, Yamamoto V, Yu C, et al. Infrared thermal imaging: a review of the literature and case report. NeuroImage. 2009;47: T154–T162.
[73] Nishikawa K, Matsudaira H, Suzuki H, et al. Intraoperative thermal imaging in esophageal replacement: its use in the assessment of gastric tube viability. Surg Today. 2006;36(9):802–806.
[74] Santos HDA, Ximendes EC, Iglesias-de la Cruz M del C, et al. In vivo early tumor detection and diagnosis by infrared luminescence transient nanothermometry. Adv Funct Mater. 2018; 28(43):1803924.
[75] Kolosnjaj-Tabi J, Di Corato R, Lartigue L, et al. Heat-generating iron oxide nanocubes: subtle "destructurators" of the tumoral microenvironment. ACS Nano. 2014;8(5):4268–4283.
[76] Rodrigues HF, Capistrano G, Mello FM, et al. Precise determination of the heat delivery during in vivo magnetic nanoparticle hyperthermia with infrared thermography. Phys Med Biol. 2017; 62(10):4062–4082.

[77] Hadadian Y, Uliana JH, Oliveira Carneiro AA, et al. A novel theranostic platform: integration of magnetomotive and thermal ultrasound imaging with magnetic hyperthermia. IEEE Trans Biomed Eng. 2020. DOI: 10.1109/TBME.2020.2990873
[78] Lewis MA, Staruch RM, Chopra R. Thermometry and ablation monitoring with ultrasound. Int J Hyperthermia. 2015;31(2):163–181.
[79] Ortgies DH, Teran FJ, Rocha U, et al. Optomagnetic nanoplatforms for in situ controlled hyperthermia. Adv Funct Mater. 2018;28(11):1704434.
[80] Tay ZW, Chandrasekharan P, Chiu-Lam A, et al. Magnetic particle imaging-guided heating in vivo using gradient fields for arbitrary localization of magnetic hyperthermia therapy. ACS Nano. 2018;12(4):3699–3713.
[81] Weaver JB, Rauwerdink AM, Hansen EW. Magnetic nanoparticle temperature estimation. Med Phys. 2009;36(5):1822–1829.
[82] Mahnken AH, Bruners P. CT thermometry: will it ever become ready for use? Int J Clin Pract. 2011;65:1–2.
[83] Fani F, Schena E, Saccomandi P, et al. CT-based thermometry: an overview. Int J Hyperthermia. 2014;30(4):219–227.
[84] Saccomandi P, Schena E, Silvestri S. Techniques for temperature monitoring during laser-induced thermotherapy: an overview. Int J Hyperthermia. 2013;29(7):609–619.
[85] Oh J, Feldman MD, Kim J, et al. Detection of magnetic nanoparticles in tissue using magneto-motive ultrasound. Nanotechnology. 2006;17(16):4183–4190.
[86] Dhavalikar R, Rinaldi C. Theoretical predictions for spatially-focused heating of magnetic nanoparticles guided by magnetic particle imaging field gradients. J Magn Magn Mater. 2016;419:267–273.
[87] Wells J, Löwa N, Paysen H, et al. Probing particle-matrix interactions during magnetic particle spectroscopy. J Magn Magn Mater. 2019;475:421–428.
[88] Fatima A, Kratkiewicz K, Manwar R, et al. Review of cost reduction methods in photoacoustic computed tomography. Photoacoustics. 2019;15:100112–100137.
[89] Capistrano G, Rodrigues HF, Zufelato N, et al. Non-invasive intratumoral thermal dose determination during in vivo magnetic nanoparticle hyperthermia: combining surface temperature measurements and computer simulations. Manuscript submitted for publication. 2020.
[90] Dewhirst MW, Viglianti BL, Lora-Michiels M, et al. Basic principles of thermal dosimetry and thermal thresholds for tissue damage from hyperthermia. Int J Hyperthermia. 2003;19(3):267–294.
[91] van Rhoon G, Pearce J, Corry P, et al. The house believes that measurement of thermal dose is essential for thermal therapy. 12th International Congress of Hyperthermic Oncology. New Orleans, LA: 2016.
[92] Sapareto SA, Hopwood LE, Dewey WC, et al. Effects of hyperthermia on survival and progression of Chinese hamster ovary cells. Cancer Res. 1978;38(2):393–400.
[93] Perez CA, Sapareto SA. Thermal dose expression in clinical hyperthermia and correlation with tumor response/control. Cancer Res. 1984;44(10 Suppl):4818s–4825s.
[94] Sapareto SA, Dewey WC. Thermal dose determination in cancer therapy. Int J Radiat Oncol. 1984;10(6):787–800.(84)90379-1.
[95] Pearce JA. Comparative analysis of mathematical models of cell death and thermal damage processes. Int J Hyperthermia. 2013;29(4):262–280.
[96] Yarmolenko PS, Moon EJ, Landon C, et al. Thresholds for thermal damage to normal tissues: An update. Int J Hyperthermia. 2011;27(4):320–343.
[97] Dewey WC. Arrhenius relationships from the molecule and cell to the clinic. Int J Hyperthermia. 2009;25(1):3–20.
[98] Field SB, Morris CC. The relationship between heating time and temperature: its relevance to clinical hyperthermia. Radiother Oncol J Eur Soc Ther Radiol Oncol. 1983;1(2):179–186.
[99] Pearce JA. Relationship between Arrhenius models of thermal damage and the CEM 43 thermal dose. In: Ryan TP, editor. 2009. p. 718104.
[100] Moritz AR, Henriques FC. Studies of thermal injury: II. The relative importance of time and surface temperature in the causation of cutaneous burns. Am J Pathol. 1947;23(5):695–720.
[101] Feng Y, Tinsley Oden J, Rylander MN. A two-state cell damage model under hyperthermic conditions: theory and in vitro experiments. J Biomech Eng. 2008;130(4):041016.
[102] Pearce JA. Improving accuracy in Arrhenius models of cell death: adding a temperature-dependent time delay. J Biomech Eng. 2015;137(12):121006.
[103] Gilchrist RK, Medal R, Shorey WD, et al. Selective inductive heating of lymph nodes. Ann Surg. 1957;146(4):596–606.
[104] Ivkov R. Magnetic nanoparticle hyperthermia: a new frontier in biology and medicine? Int J Hyperthermia. 2013;29(8):703–705.
[105] Danhier F. To exploit the tumor microenvironment: since the EPR effect fails in the clinic, what is the future of nanomedicine? J Control Release. 2016;244(Pt A):108–121.
[106] Matsumura Y, Maeda H. A new concept for macromolecular therapeutics in cancer chemotherapy: mechanism of tumoritropic accumulation of proteins and the antitumor agent smancs. Am Assoc Cancer Res. 1986;46:6387–6392.
[107] Maeda H, Tsukigawa K, Fang J. A retrospective 30 years after discovery of the enhanced permeability and retention effect of solid tumors: next-generation chemotherapeutics and photodynamic therapy-problems, solutions, and prospects. Microcirculation. 2016;23(3):173–182.
[108] Petros RA, DeSimone JM. Strategies in the design of nanoparticles for therapeutic applications. Nat Rev Drug Discov. 2010;9(8):615–627.
[109] Kozissnik B, Bohorquez AC, Dobson J, et al. Magnetic fluid hyperthermia: advances, challenges, and opportunity. Int J Hyperthermia. 2013;29(8):706–714.
[110] Sindhwani S, Syed AM, Ngai J, et al. The entry of nanoparticles into solid tumours. Nat Mater. 2020;19(5):566–575.
[111] Gratton SEA, Ropp PA, Pohlhaus PD, et al. The effect of particle design on cellular internalization pathways. Proc Natl Acad Sci USA. 2008;105(33):11613–11618.
[112] Rabin Y. Is intracellular hyperthermia superior to extracellular hyperthermia in the thermal sense? Int J Hyperthermia. 2002;18(3):194–202.
[113] Williams DF. On the mechanisms of biocompatibility. Biomaterials. 2008;29(20):2941–2953.
[114] Williams DF. There is no such thing as a biocompatible material. Biomaterials. 2014;35(38):10009–10014.
[115] Malvindi MA, De Matteis V, Galeone A, et al. Toxicity assessment of silica coated iron oxide nanoparticles and biocompatibility improvement by surface engineering. PLoS ONE. 2014;9(1):e85835.
[116] Reddy LH, Arias JL, Nicolas J, et al. Magnetic nanoparticles: design and characterization, toxicity and biocompatibility, pharmaceutical and biomedical applications. Chem Rev. 2012;112(11):5818–5878.
[117] Huang D-M, Chung T-H, Hung Y, et al. Internalization of mesoporous silica nanoparticles induces transient but not sufficient osteogenic signals in human mesenchymal stem cells. Toxicol Appl Pharmacol. 2008;231(2):208–215.
[118] Jain TK, Reddy MK, Morales MA, et al. Biodistribution, clearance, and biocompatibility of iron oxide magnetic nanoparticles in rats. Mol Pharm. 2008;5(2):316–327.
[119] Weissleder R, Stark D, Engelstad B, et al. Superparamagnetic iron oxide: pharmacokinetics and toxicity. AJR Am J Roentgenol. 1989;152(1):167–173.
[120] Bourrinet P, Bengele HH, Bonnemain B, et al. Preclinical safety and pharmacokinetic profile of ferumoxtran-10, an ultrasmall superparamagnetic iron oxide magnetic resonance contrast agent. Invest Radiol. 2006;41(3):313–324.
[121] Weissleder R, Nahrendorf M, Pittet MJ. Imaging macrophages with nanoparticles. Nat Mater. 2014;13(2):125–138.
[122] Kut C, Zhang Y, Hedayati M, et al. Preliminary study of injury from heating systemically delivered, nontargeted dextran-

superparamagnetic iron oxide nanoparticles in mice. Nanomedicine (Lond). 2012;7(11):1697–1711.
[123] Yu M, Zheng J. Clearance pathways and tumor targeting of imaging nanoparticles. ACS Nano. 2015;9(7):6655–6674.
[124] Quini CC, Matos JF, Próspero AG, et al. Renal perfusion evaluation by alternating current biosusceptometry of magnetic nanoparticles. J Magn Magn Mater. 2015;380:2–6.
[125] Sousa-Junior AA, Mendanha SA, Carrião MS, et al. Predictive model for delivery efficiency: erythrocyte membrane-camouflaged Magnetofluorescent Nanocarriers Study. Mol Pharm. 2020;17(3):837–851.
[126] U.S. Food and Drug Administration - FDA. MRI (Magnetic Resonance Imaging). FDA 2019. [cited 2020 June 19]. https://www.fda.gov/radiation-emitting-products/medical-imaging/mri-magnetic-resonance-imaging
[127] International Commission on Non-Ionizing Radiation Protection (ICNIRP). Guidelines for limiting exposure to electromagnetic fields (100 kHz to 300 GHz). Health Phys. 2020;118:483–524.
[128] Oleson JR. A review of magnetic induction methods for hyperthermia treatment of cancer. IEEE Trans Biomed Eng. 1984;31(1):91–97.
[129] Cheshire WP. Thermoregulatory disorders and illness related to heat and cold stress. Auton Neurosci. 2016;196:91–104.
[130] Young JH, Wang M-T, Brezovich IA. Frequency/depth-penetration considerations in hyperthermia by magnetically induced currents. Electron Lett. 1980;16(10):358.
[131] van Rhoon GC, Samaras T, Yarmolenko PS, et al. CEM43 °C thermal dose thresholds: a potential guide for magnetic resonance radiofrequency exposure levels? Eur Radiol. 2013;23(8):2215–2227.
[132] Andreuccetti D, Fossi R, Petrucci C. An Internet resource for the calculation of the dielectric properties of body tissues in the frequency range 10 Hz - 100 GHz. *Based on data published by Gabriel C et al. in 1996*. 1997. [cited 2017 March 7]. http://niremf.ifac.cnr.it/tissprop/
[133] Gabriel C, Gabriel S, Corthout E. The dielectric properties of biological tissues: I. Literature survey. Phys Med Biol. 1996;41(11):2231–2249.
[134] Gabriel S, Lau RW, Gabriel C. The dielectric properties of biological tissues: II. Measurements in the frequency range 10 Hz to 20 GHz. Phys Med Biol. 1996;41(11):2251–2269.
[135] Gabriel S, Lau RW, Gabriel C. The dielectric properties of biological tissues: III. Parametric models for the dielectric spectrum of tissues. Phys Med Biol. 1996;41(11):2271–2293.
[136] Wust P, Gneveckow U, Johannsen M, et al. Magnetic nanoparticles for interstitial thermotherapy-feasibility, tolerance and achieved temperatures. Int J Hyperthermia. 2006;22(8):673–685.
[137] Singh MP, Sethuraman SN, Ritchey J, et al. In-situ vaccination using focused ultrasound heating and anti-CD-40 agonistic antibody enhances T-cell mediated local and abscopal effects in murine melanoma. Int J Hyperthermia. 2019;36(sup1):64–73.
[138] Wennerberg E, Lhuillier C, Vanpouille-Box C, et al. Barriers to radiation-induced in situ tumor vaccination. Front Immunol. 2017;8:211–229.
[139] Ngwa W, Irabor OC, Schoenfeld JD, et al. Using immunotherapy to boost the abscopal effect. Nat Rev Cancer. 2018;18(5):313–322.
[140] Daguenet E, Louati S, Wozny A-S, et al. Radiation-induced bystander and abscopal effects: important lessons from preclinical models. Br J Cancer. 2020. Doi:10.1038/s41416-020-0942-3
[141] Toraya-Brown S, Fiering S. Local tumour hyperthermia as immunotherapy for metastatic cancer. Int J Hyperthermia. 2014;30(8):531–539.
[142] Sheen MR, Fiering S. *In situ* vaccination: harvesting low hanging fruit on the cancer immunotherapy tree. Wiley Interdiscip Rev Nanomed Nanobiotechnol. 2019;11(1):e1524.
[143] Fiering SN, Evans S. Introduction to thermal therapy and immunotherapy: at the crossroads of new discovery. Int J Hyperthermia. 2019;36(sup1):1–2.
[144] Carrião MS, Bakuzis AF. Mean-field and linear regime approach to magnetic hyperthermia of core-shell nanoparticles: can tiny nanostructures fight cancer? Nanoscale. 2016;8(15):8363–8377.
[145] Issels RD, Lindner LH, Verweij J, et al. Neo-adjuvant chemotherapy alone or with regional hyperthermia for localised high-risk soft-tissue sarcoma: a randomised phase 3 multicentre study. Lancet Oncol. 2010;11(6):561–570.
[146] Horsman MR, Overgaard J. The impact of hypoxia and its modification of the outcome of radiotherapy. J Radiat Res. 2016;57(S1):i90–i98.
[147] Aquino VRR, Figueiredo LC, Coaquira JAH, et al. Magnetic interaction and anisotropy axes arrangement in nanoparticle aggregates can enhance or reduce the effective magnetic anisotropy. J Magn Magn Mater. 2020;498:166170.
[148] Aquino VRR, Vinícius-Araújo M, Shrivastava N, et al. Role of the fraction of blocked nanoparticles on the hyperthermia efficiency of Mn-based ferrites at clinically relevant conditions. J Phys Chem C. 2019;123(45):27725–27734.
[149] MagForce AG, Inc. Since 2011, MagForce AG holds the European CE certificate and thus official approval of NanoTherm® therapy for the treatment of brain tumors in Germany and all member states of the European Union. n.d. [cited 2020 April 10]. https://magforce.com
[150] Southern P, Pankhurst QA. Commentary on the clinical and preclinical dosage limits of interstitially administered magnetic fluids for therapeutic hyperthermia based on current practice and efficacy models. Int J Hyperthermia. 2018;34(6):671–686.
[151] Freeman AC, Platt SR, Holmes S, et al. Convection-enhanced delivery of cetuximab conjugated iron-oxide nanoparticles for treatment of spontaneous canine intracranial gliomas. J Neurooncol. 2018;137(3):653–663.
[152] Dennis CL, Jackson AJ, Borchers JA, et al. The influence of collective behavior on the magnetic and heating properties of iron oxide nanoparticles. J Appl Phys. 2008;103(7):07A319.
[153] Lartigue L, Hugounenq P, Alloyeau D, et al. Cooperative organization in iron oxide multi-core nanoparticles potentiates their efficiency as heating mediators and MRI contrast agents. ACS Nano. 2012;6(12):10935–10949.
[154] Hugounenq P, Levy M, Alloyeau D, et al. Iron oxide monocrystalline nanoflowers for highly efficient magnetic hyperthermia. J Phys Chem C. 2012;116(29):15702–15712.
[155] Liu XL, Choo ESG, Ahmed AS, et al. Magnetic nanoparticle-loaded polymer nanospheres as magnetic hyperthermia agents. J Mater Chem B. 2014;2(1):120–128.
[156] Dennis CL, Krycka KL, Borchers JA, et al. Internal magnetic structure of nanoparticles dominates time-dependent relaxation processes in a magnetic field. Adv Funct Mater. 2015;25(27):4300–4311.
[157] Shubitidze F, Kekalo K, Stigliano R, et al. Magnetic nanoparticles with high specific absorption rate of electromagnetic energy at low field strength for hyperthermia therapy. J Appl Phys. 2015;117(9):094302.
[158] Das R, Rinaldi-Montes N, Alonso J, et al. Boosted hyperthermia therapy by combined AC magnetic and photothermal exposures in Ag/Fe_3O_4 nanoflowers. ACS Appl Mater Interfaces. 2016;8(38):25162–25169.
[159] Soleymani M, Edrissi M, Alizadeh AM. Tailoring La1-xSrxMnO3 ($0.25 \leq x \leq 0.35$) nanoparticles for self-regulating magnetic hyperthermia therapy: an in vivo study. J Mater Chem B. 2017;5(24):4705–4712.
[160] Hemery G, Genevois C, Couillaud F, et al. Monocore *vs.* multicore magnetic iron oxide nanoparticles: uptake by glioblastoma cells and efficiency for magnetic hyperthermia. Mol Syst Des Eng. 2017;2(5):629–639.
[161] Gavilán H, Sánchez EH, Brollo MEF, et al. Formation mechanism of maghemite nanoflowers synthesized by a polyol-mediated process. ACS Omega. 2017;2(10):7172–7184.
[162] Phong PT, Nam PH, Manh DH, et al. $Mn_{0.5}Zn_{0.5}Fe_2O_4$ nanoparticles with high intrinsic loss power for hyperthermia therapy. J Magn Magn Mater. 2017;433:76–83.

[163] Bender P, Fock J, Hansen MF, et al. Influence of clustering on the magnetic properties and hyperthermia performance of iron oxide nanoparticles. Nanotechnology. 2018;29(42):425705.
[164] He S, Zhang H, Liu Y, et al. Maximizing specific loss power for magnetic hyperthermia by hard-soft mixed ferrites. Small. 2018; 14(29):1800135.
[165] Bender P, Honecker D, Fernández Barquín L. Supraferromagnetic correlations in clusters of magnetic nanoflowers. Appl Phys Lett. 2019;115(13):132406.
[166] Curcio A, Silva AKA, Cabana S, et al. Iron oxide nanoflowers @ CuS hybrids for cancer tri-therapy: interplay of photothermal therapy, magnetic hyperthermia and photodynamic therapy. Theranostics. 2019;9(5):1288–1302.
[167] Del Sol-Fernández S, Portilla-Tundidor Y, Gutiérrez L, et al. Flower-like Mn-doped magnetic nanoparticles functionalized with αvβ3-integrin-ligand to efficiently induce intracellular heat after alternating magnetic field exposition, triggering glioma cell death . ACS Appl Mater Interfaces. 2019;11(30):26648–26663.
[168] Ognjanović M, Radović M, Mirković M, et al. ^{99m}Tc-, ^{90}Y-, and ^{177}Lu-labeled iron oxide nanoflowers designed for potential use in dual magnetic hyperthermia/radionuclide cancer therapy and diagnosis. ACS Appl Mater Interfaces. 2019;11(44):41109–41117.
[169] Attaluri A, Seshadri M, Mirpour S, et al. Image-guided thermal therapy with a dual-contrast magnetic nanoparticle formulation: a feasibility study. Int J Hyperthermia. 2016;32(5):543–557.
[170] Zadnik PL, Molina CA, Sarabia-Estrada R, et al. Characterization of intratumor magnetic nanoparticle distribution and heating in a rat model of metastatic spine disease. J Neurosurg Spine. 2014;20(6):740–750.
[171] Branquinho LC, Carrião MS, Costa AS, et al. Effect of magnetic dipolar interactions on nanoparticle heating efficiency: implications for cancer hyperthermia. Sci Rep. 2013;3:2887.
[172] Pavel M, Gradinariu G, Stancu A. Study of the optimum dose of ferromagnetic nanoparticles suitable for cancer therapy using MFH. IEEE Trans Magn. 2008;44(11):3205–3208.
[173] Pavel M, Stancu A. Study of the optimum injection sites for a multiple metastases region in cancer therapy by using MFH. IEEE Trans Magn. 2009;45(10):4825–4828.
[174] Pavel M, Stancu A. Ferromagnetic nanoparticles dose based on tumor size in magnetic fluid hyperthermia cancer therapy. IEEE Trans Magn. 2009;45(11):5251–5254.
[175] Pearce JA, Petryk AA, Hoopes PJ. Numerical model study of in vivo magnetic nanoparticle tumor heating. IEEE Trans Biomed Eng. 2017;64(12):2813–2823.
[176] Li J, Yao H, Lei Y, et al. Numerical simulation of magnetic fluid hyperthermia based on multiphysics coupling and recommendation on preferable treatment conditions. Curr Appl Phys. 2019; 19(9):1031–1039.
[177] Tang Y, Flesch RCC, Jin T. Numerical method to evaluate the survival rate of malignant cells considering the distribution of treatment temperature field for magnetic hyperthermia. J Magn Magn Mater. 2019;490:165458.
[178] Pennes HH. Analysis of tissue and arterial blood temperatures in the resting human forearm. J Appl Physiol. 1948;1(2):93–122.
[179] Wissler EH. Pennes' 1948 paper revisited. J Appl Physiol. 1998; 85(1):35–41.
[180] Javidi M, Heydari M, Karimi A, et al. Evaluation of the effects of injection velocity and different gel concentrations on nanoparticles in hyperthermia therapy. J Biomed Phys Eng. 2014;4(4): 151–162.
[181] Kandala SK, Liapi E, Whitcomb LL, et al. Temperature-controlled power modulation compensates for heterogeneous nanoparticle distributions: a computational optimization analysis for magnetic hyperthermia. Int J Hyperthermia. 2019;36(1):115–129.
[182] Johannsen M, Gneveckow U, Thiesen B, et al. Thermotherapy of prostate cancer using magnetic nanoparticles: feasibility, imaging, and three-dimensional temperature distribution. Eur Urol. 2007;52(6):1653–1661.
[183] Lang J, Erdmann B, Seebass M. Impact of nonlinear heat transfer on temperature control in regional hyperthermia. IEEE Trans Biomed Eng. 1999;46(9):1129–1138.
[184] Solberg OV, Lindseth F, Torp H, et al. Freehand 3D ultrasound reconstruction algorithms-a review. Ultrasound Med Biol. 2007; 33(7):991–1009.
[185] Weissleder R, Pittet MJ. Imaging in the era of molecular oncology. Nature. 2008;452(7187):580–589.
[186] Rocha U, Upendra Kumar K, Jacinto C, et al. N^{d3+} doped LaF_3 nanoparticles as self-monitored photo-thermal agents. Appl Phys Lett. 2014;104(5):053703.
[187] Shah J, Park S, Aglyamov S, et al. Photoacoustic imaging and temperature measurement for photothermal cancer therapy. J Biomed Opt. 2008;13(3):034024.
[188] Marques JP, Simonis FFJ, Webb AG. Low-field MRI: an MR physics perspective. J Magn Reson Imaging. 2019;49(6):1528–1542.
[189] Gleich B, Weizenecker J. Tomographic imaging using the nonlinear response of magnetic particles. Nature. 2005;435(7046): 1214–1217.
[190] Goodwill PW, Saritas EU, Croft LR, et al. X-Space MPI: magnetic nanoparticles for safe medical imaging. Adv Mater. 2012;24(28): 3870–3877.
[191] Hensley D, Tay ZW, Dhavalikar R, et al. A theranostic platform for localized magnetic fluid hyperthermia and magnetic particle imaging. Proceedings of the SPIE 10066, Energy-based Treatment of Tissue and Assessment IX, 1006603; 2017.
[192] Bender P, Fock J, Frandsen C, et al. Relating magnetic properties and high hyperthermia performance of iron oxide nanoflowers. J Phys Chem C. 2018;122(5):3068–3077.
[193] Graeser M, Thieben F, Szwargulski P, et al. Human-sized magnetic particle imaging for brain applications. Nat Commun. 2019;10(1):1936.
[194] Foiret J, Ferrara KW. Spatial and temporal control of hyperthermia using real time ultrasonic thermal strain imaging with motion compensation, phantom study. PLoS One. 2015;10(8): e0134938.